UNIVERSITY OF CALIFORNIA

SANTA CRUZ

Delivering Carbon Monoxide from a Porous Material with an Entrapped Photoactive Manganese Carbonyl

a thesis submitted in partial satisfaction
of the requirements for the degree of

MASTER OF SCIENCE

in

Chemistry

by

Il Gu (Howard) Han

June 2013

The thesis of Il Gu (Howard) Han
is approved:

_____
Professor Scott RJ Oliver

_____
Professor Pradip K Mascharak

_____
Professor Yat Li

_____
Tyrus Miller
Vice Provost and Dean of Graduate Studies

TABLE OF CONTENTS

LIST OF FIGURES

ABSTRACT

Il Gu (Howard) Han

DELIVERING CARBON MONOXIDE FROM A POROUS MATERIAL
WITH AN ENTRAPPED PHOTOACTIVE MANGANESE CARBONYL

Carbon monoxide (CO), typically known as a toxic gas has gained attention since the discovery of its role in cell signaling, making it a potential therapeutic agent. However, it has showed difficulties in direct clinical use due to its concentration-dependent toxicity. In 2002, carbon monoxide releasing materials (CORMs) were first introduced as a potential CO delivery system. Use of CORMs enabled localized administration of CO. This not only reduced the risk of exposing CO to the normal cells, it increased the efficacy by maintaining high dose at the target site.

In this study, we have developed a new CO delivery system that further improves overall efficiency. Our design consists of photoactive manganese carbonyl CORM encapsulated within mesoporous silicate nanoparticles (MSN). It has shown several advantages over raw administration of CORM. It was able to hold CO with minimum leakage, and released sufficient amounts of CO upon irritation with broad UV light at fast rate. MSN also showed promising cell uptake and cell viability.

ACKNOWLEDGEMENTS

FOR AIUR

CHAPTER 1

INTRODUCTION

Carbon monoxide (CO), a small gaseous molecule that is a little lighter than air, is known as a "silent killer" due to its colorless, odorless, and tasteless character. While it is very difficult for humans to detect its presence, exposures at even 100 ppm can cause damage.[1-3]

CO binds very strongly to the iron atoms in hemoglobin and can significantly reduce the oxygen-carrying capacity, leading to tissue hypoxia. The brain and the heart can be severely affected if carboxyhemoglobin (CO-Hb) level exceeds 80%.[1,2] Because of this well-known toxic character, CO has been overlooked for many years and did not attract much research. CO received its attention as NO, a molecule with similar structure and molecular size, was recognized as a cell signaling agent. Because of the chemical similarity between those two molecules, it brought up new possibilities for CO's biological role.[4] It was later discovered that CO also induces cell signaling, resulting in anti-inflammatory, anti-apoptotic, anti-proliferative, and anti-thombosis effects, showing its potentials for therapeutic applications.

Because of its gaseous form, CO showed difficulties for direct clinical use. In its early stage, CO was delivered through the lungs as a mixture with air, which makes the whole body exposed to it.[5] Because overdose of CO can damage the normal cells, a constant monitoring of carbonmonoxyhemoglobin level was required.

This disadvantage led to a development of carbon monoxide releasing

materials, or CORMs. A CORM is typically a metal carbonyl that is stable enough to store CO, yet releases it when introduced into the body. The biggest advantage gained from the use of a CORM is localized administration. When the CO source is within the target area, dispersion of CO within the body is confined, reducing the risk of damaging the surrounding normal cells and increase in its therapeutic efficacy.

In order to further improve CO delivery performance, we have developed a system consisting of manganese based photoactive CORM encapsulated within mesoporous silicate nanoparticles. Drug encapsulation system has been a popular choice due to its many advantages such as biocompatibility, ease and reasonably cheap method to prepare, and ease in modifying the textural and surface properties.[6] In this work, we showed the following aspects of our system: 1) Photocontrolled release of CO; 2) High performance in cell uptake and cell viability; 3) Minimum leakage of CORM from the material; and 4) Consistent and sufficient loading capacity.

CHAPTER 2

CARBON MONOXIDE

In this chapter, general background of CO and its biological relevance are discussed. Cell signaling mechanism of CO and the following physiological effects are briefly reviewed.

2.1 ENVIRONMENTAL AND ENDOGENOUS SOURCES

CO is commonly produced as a byproduct of incomplete combustion of organic matter. In nature, volcanic emissions, wild fires, and the respiration processes of living aerobic organism are the examples of atmospheric CO sources. A large portion of the atmospheric CO is from man-made sources. According to United States Environmental Protection Agency (EPA), those sources include gas space heaters, leaking chimneys and furnaces, wood stoves, automobile, and even tobacco smoke. Average levels of CO in homes without gas stoves vary from 0.5 to 5 ppm, but with stoves that are poorly installed, it could increase to 30 ppm or higher. Starting from 35 ppm, it starts to show symptoms such as headache and dizziness with prolonged exposure.

CO also occurs naturally within the body. In the late 1960s, it was first proposed that the endogenous source of CO production is due to heme oxygenase (HO)[7] In later years, inducible isoforms of HO, HO-1[8], HO-2[9], and HO-3[10], were identified. The pathway of heme metabolism is described in Figure 1. HO oxidizes heme with 3 mols of O_2 and protonated form of nicotinamide adenine dinucleotide

phosphate (NADPH), and produces CO and Fe(II), cleaved from heme. The rate of endogenous CO production in humans was first estimated by blood carboxyhemoglobin analyses to ~ 0.42 ml/h.[11]

In the absence of significant ambient CO, the majority of blood CO-Hb arises from endogenous production, corresponding to blood CO levels of 0.4%-1%[12] Environmental background factor also can increase the CO level. For example, cigarette smokers display an average range of 3-8% CO-Hb levels.[13] The level of CO concentration also may increase as a product of inflammation, physical stress, or environmental exposure with a variety of agents[13] The purpose of endogenous CO will be discussed in Section 2.3.

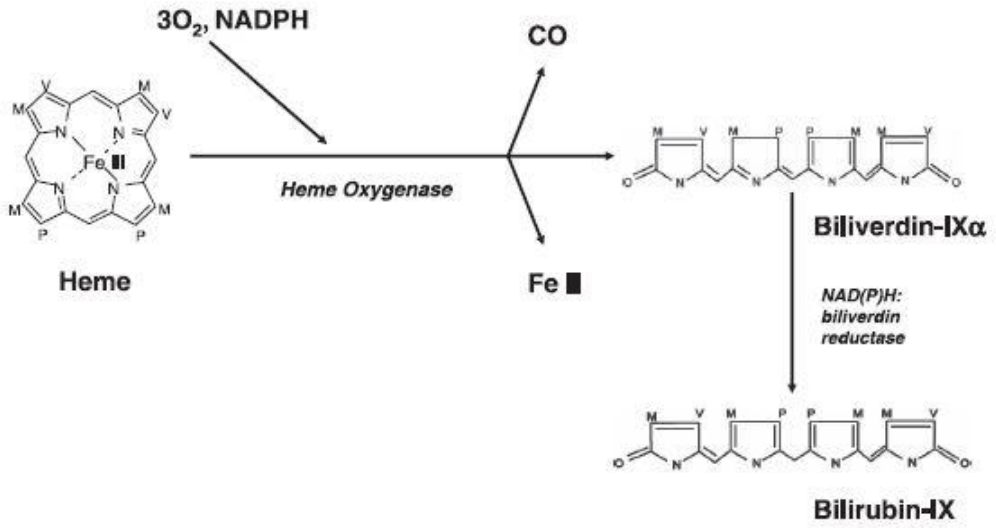

Figure 1. The pathway of heme metabolism.[13]

2.2 TOXICITY

As mentioned in Chapter 1, CO has no color, odor, or taste, which makes it very hard to detect its presence for humans. Although natural sources of CO do

not contribute much to the overall atmospheric CO level, human-caused sources of CO, such as poorly installed stoves in a confined area can rapidly increase the CO concentration which will lead to a series of symptoms. Goldstein *et al*. reported a study of the relationship between CO concentration, CO-Hb level and associated symptom, shown in Table 1.

Table 1. CO concentrations, CO-Hb levels, and associated symptoms[3]

Carbon monoxide concentration (ppm)	CO-Hb level (%)	Signs and symptoms
35	<10	Headache and dizziness within 6 to 8 h of constant exposure
100	>10	Slight headache in 2 to 3 h
200	20	Slight headache within 2 to 3 h; loss of judgment
400	25	Frontal headache within 1 to 2 h
800	30	Dizziness, nausea, and convulsions within 45 min; insensible within 2 h
1,600	40	Headache, tachycardia, dizziness, and nausea within 20 min; death in less than 2 h
3,200	50	Headache, dizziness, and nausea in 5 to 10 min; death within 30 min
6,400	60	Headache and dizziness in 1 to 2 min; convulsions, respiratory arrest, and death in less than 20 min
12,800	>70	Death in less than 3 min

It was first reported in 1912 that CO can reversibly bind to hemoglobin.[3] It has been reported that the affinity of CO for Hb is 246 times higher than of O_2 in blood, making oxygen unable to bind to Hb. Also, due to the cooperative binding characteristic of Hb, the oxygens that were already bound to Hb would be forced to be released. Prolonged exposure will cause increase in the level of CO-

Hb in the blood, causing higher damage to the body as described in Table 1.

2.3 CO-DEPENDENT CELL SIGNALING

Studies revealed that CO induces cellular signaling effects, leading to anti-inflammation, anti-apoptosis, anti-proliferation, and anti-thrombosis effects.[13] In Figure 2, schematic map of signaling pathways of CO and its physiological effects are shown. In this chapter, each effect will be briefly discussed.

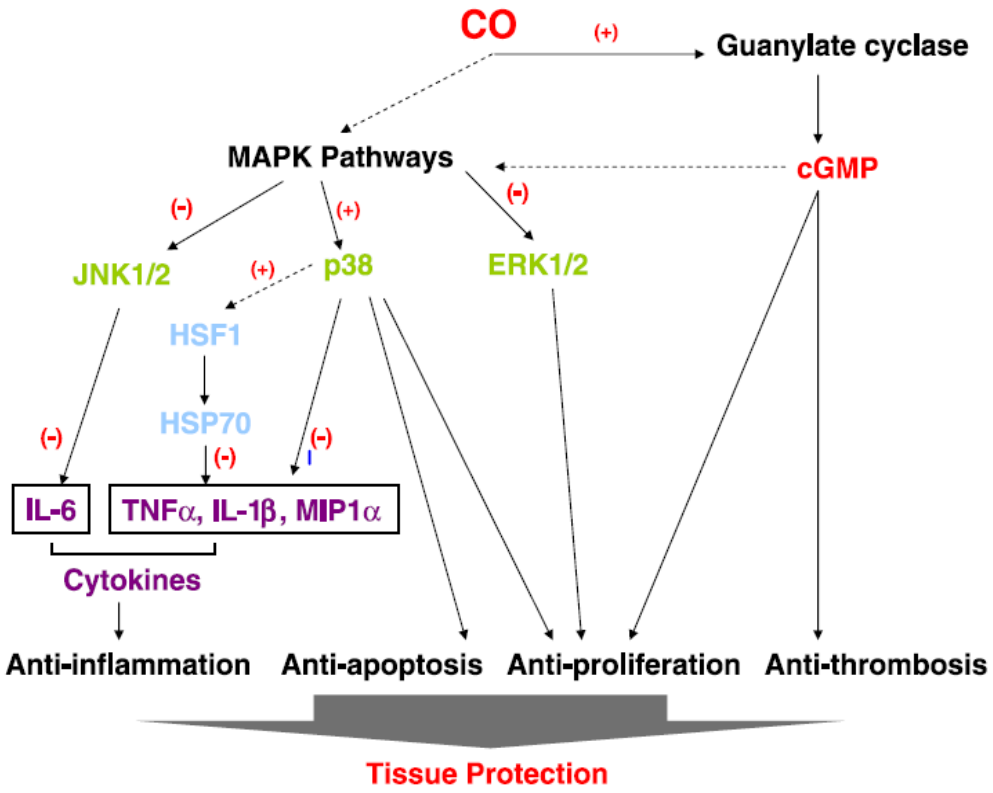

Figure 2. Potential signaling pathways activated by CO leading to tissue protection.

When CO is endogenously produced from HO activity, it can bind to the

heme iron of sGC (soluble guanylyl cyclase), which leads to cGMP (cyclic guanosine monophosphate) production in vascular smooth muscle cells (VSMCs).[14] Even when CO is directly treated on VSMC, increase in cellular cGMP levels is also observed. cGMT is known to regulate ion channel conductance, glycogeneolysis, and cell relaxation. Relaxation of smooth muscle cells within the blood vessels widens the vessel, which is also called vasodilation. With vasodilated blood vessels, the flow of the blood increases. Thus, by generating more cGMT, CO ultimately works as an anti-thrombotic agent.

While high concentration of CO leads to cell apoptosis, the opposite effect is observed at low concentration. It was shown that either an exogenous source of CO or the CO from overexpression of HO-1 both inhibited TNF-α that leads to apoptosis.[16,17] However, not all cell models show anti-apoptotic effects from the presence of CO. A report suggested that a proapoptotic result was shown with CO in endothelial cells even at low concentration.[17]

The anti-inflammatory effect of CO was tested by inhibiting some of the known proinflammatory cytokines. In the studies from Otterbein *et al.*[18], inhibition of TNF-α, Il-1β, MIP-1β, MIP 2, and Il-10 with CO were tested toward less inflammatory damage. Each type of cytokines was tested with 4 different conditions: air, CO, Lipopolysaccharide (LPS), and a mixture of CO and LPS (Figure 3). LPS promotes proinflammatory cytokineses as listed previously. When LPS was treated with CO, cytokinese production was lowered except for MIP 2 and IL-2.

Lastly, there are several different studies reported on the anti-proliferative effect of CO. In the study by Otterbein *et al*., they proved that treating smooth

muscle cells with CO can induce $p21^{Waf1/Cip1}$ expression.[19] $p21^{Waf1/Cip1}$ is known to inhibit cell cycle prokinases which causes SMC proliferation. They observe that anti-proliferative effect of CO diminished after removing $p21^{Waf1/Cip1}$ from the sample. Another case of anti-proliferation induced by CO was reported in a model of CD3 antibody-induced T-cell proliferation. Leukemia cell lines and primary cultured T lymphocytes increase caspase activity during cellular proliferation.[20] Treatment of lymphosytes with anti-CD3 antibody stimulated cellular proliferation in primary cell cultures. When it was treated with CO (250 ppm), there was a decrease in cellular proliferation (Figure 4).

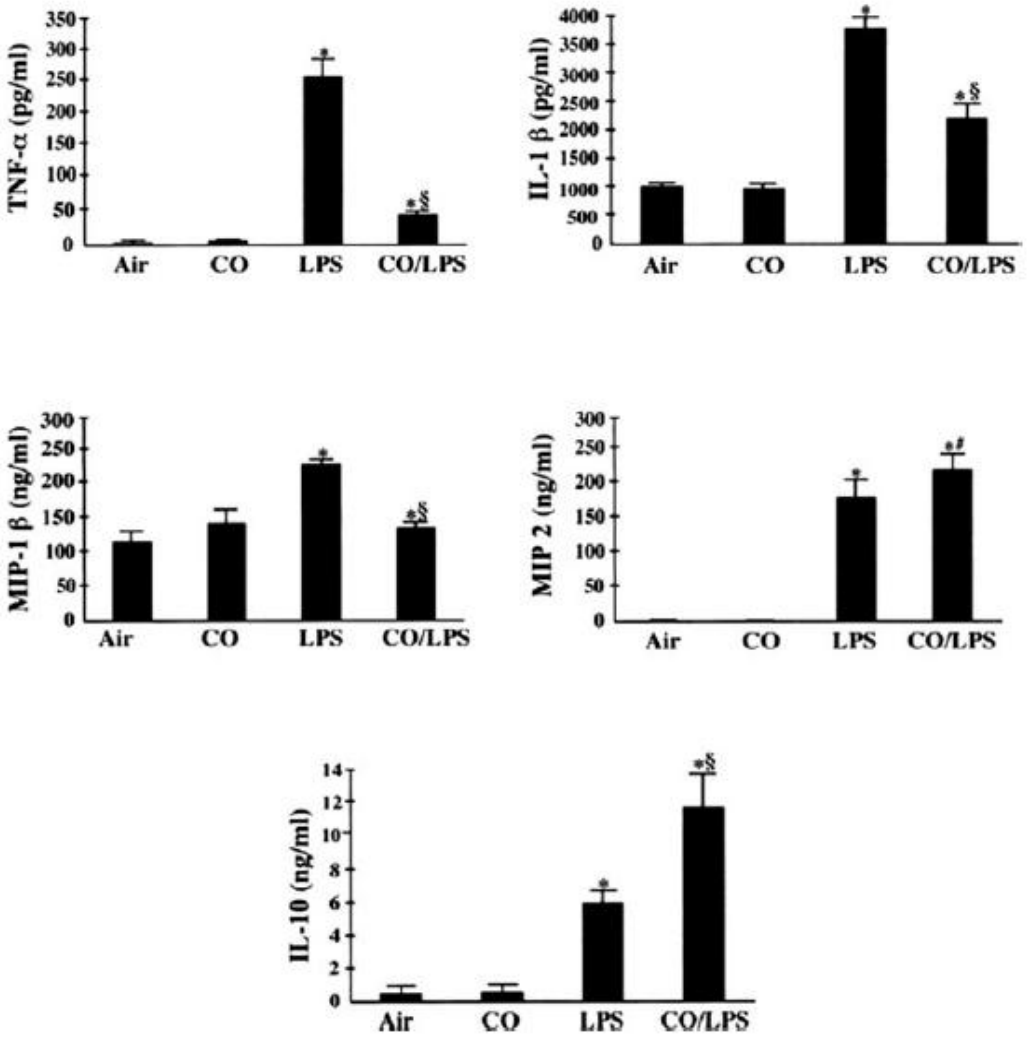

Figure 3. Effects of CO on LPS-induced cytokine production *in vitro*. RAW 264.7 macrophage was pretreated with 250 ppm CO before being treated with LPS. Culture media was collected and analyzed by Enzyme-linked immunosorbent assay(ELISA).

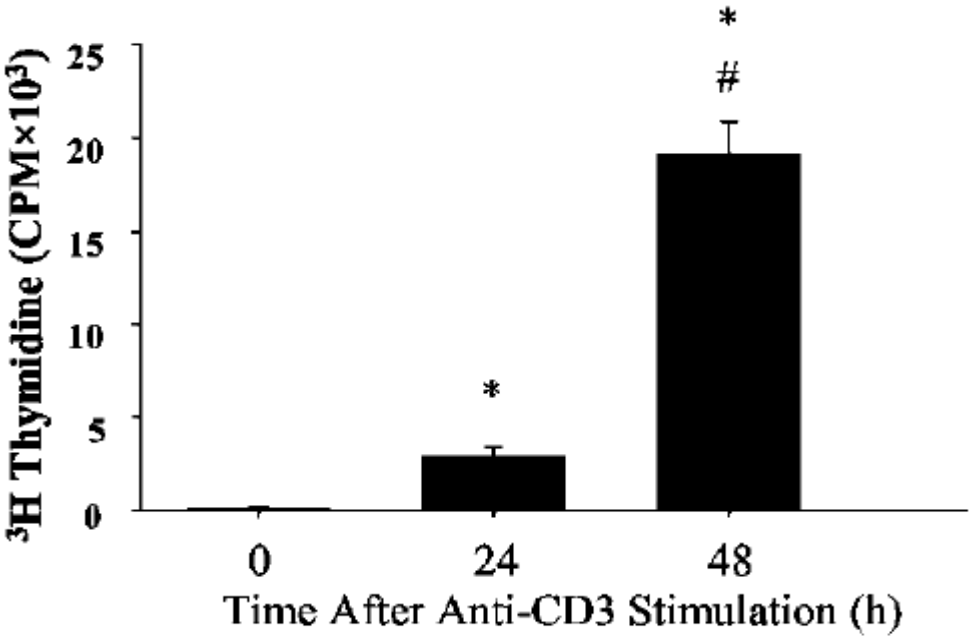

Figure 4. CD3 stimulates primary T lymphocytes to proliferate. Primary spleen T lymphocytes were stimulated to proliferate with immobilized anti-CD3. Proliferation was assessed at 24- and 48-h time points after stimulation by [^{3}H]TdR incorporation.

CHAPTER 3

CARBON MONOXIDE RELEASING MATERIALS (CORMS)

While the clinical value of CO has been proven, there are still disadvantages that reduce the practicality of CO on its own. As discussed in Chapter 2, direct injection of CO to the lungs leaves the enitre body exposed. This reduces its clinical efficacy. For example, inflammation occurs usually in a part of the body that requires localized administration. CO molecules distributed to the area other than the target site are not only wasted, but also can put the normal cells in danger if the dosage is not monitored constantly. Use of a carbon monoxide releasing material, or CORM can overcome this disadvantage. Use of a CORM allows a systemic route of medication, keeping high CO concentration at the target site, reducing unwanted damage to the surrounding cells.

Formally, transition metal carbonyl complexes have been used in catalysis and synthetic chemistry.[21] In 2002, CORMs were first introduced as potential pharmaceutical agents.[22] The first CORM-1 (Mn_2CO_{10}) and CORM-2 [$Ru(CO)_3Cl$-dimer] were tested in vasodilatation and hypotension *in vivo*. However, those two CORMs had several disadvantages. Both CORM-1 and CORM-2 were insoluble in aqueous media, which reduces its potentials under in physiological conditions. CORM-2 could be used in a solution of DMSO, but it only released to myoglobin around 0.9 mol CO/mol of [$Ru(CO)_3Cl$-dimer].[22,24]

In this chapter, a report on CORM-3 by Clark *et al*.[24] will be examined as an example. Also, the photoactive manganese carbonyl CORM, or [$Mn(pqa)(CO)_3]ClO_4$] will be discussed.

3.1. CORM-3

CORM-3 or $Ru(Cl)(CO)_3$(glycinate) is the first water soluble metal carbonyl that releases CO under physiological conditions.[24] While the previous CORM-1 and CORM-2 were designed for synthetic application, CORM-3 was specifically designed to be used for medical purposes. Clark *et al*. have tested three aspects: 1) protection against hypoxia-reoxygenation and oxidative stress, 2) cardioprotective effects against myocaardial ischemia-reperfusion injury, and 3) prevention of cardiac allograft rejection in mice.

In the first experiment, H9c2 cells were exposed to hypoxia for 24 hours, followed by reoxygenation for 6 hours. For a controlled group with no special treatment, there was about 70% loss in cell viability. They have prepared other groups of specimen with CORM-3 and iCORM-3, which is the inactivated CORM that cannot release CO. Additional experiments were performed with CORM-3 for 5-hydroxydecanoic acid (5-HD). It is an inhibitor for mitochontrial ATP-dependent potassium ($mitoK_{ATP}$), and the purpose in this experiment was to see the relation between CO and the $mitoK_{ATP}$ channel. Figure 5 shows the comparison in cell viability after hypoxia-reoxygenation in cardiomyocytes. It is evident that the use of CORM-3 dramatically increased the cell viability compared to other groups. However, it is also notable that the result is concentration dependent. With CORM-3 concentration at 10 μM, there was not much improvement in cell viability. They also reported that even when CORM-3 was introduced only during 6 hours of reoxygenation period, there was cell viability improvement. (Figure 5).

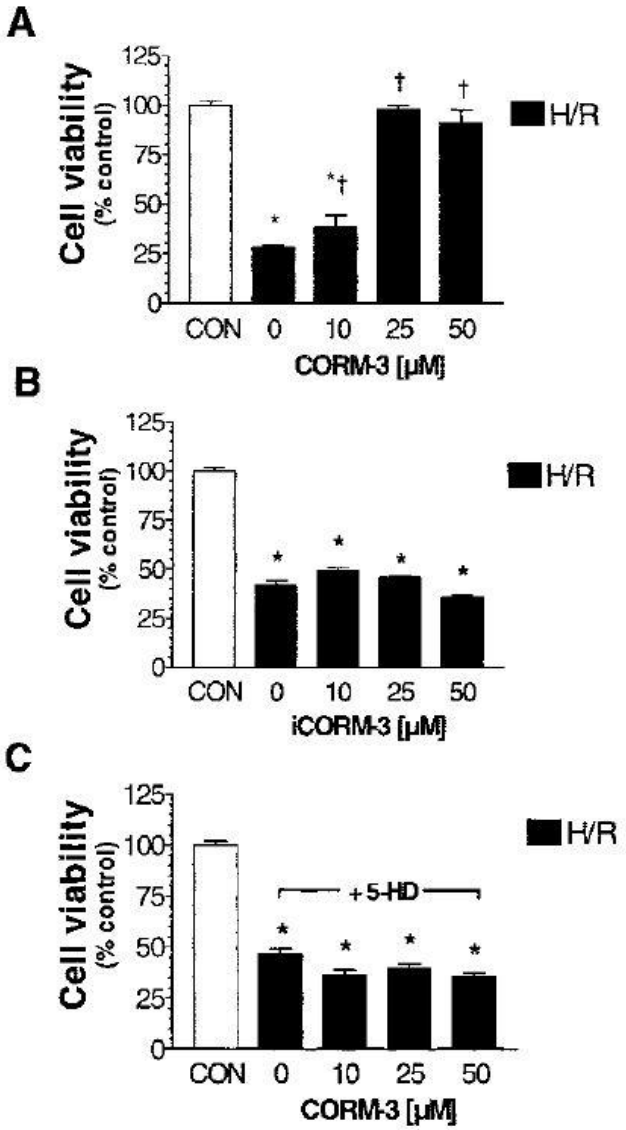

Figure 5. Cytoprotective effects of CORM-3 against hypoxia-reoxygenation (H/R) in cardiomyocytes. Cardiomyocytes were exposed to hypoxia for 24 hours in the presence of CORM-3 (A), iCORM-3 (B), or CORM-3 plus 50 μM 5-HD (C). Cells were then reoxygenated and cell viability determined after 6 hours. Control cells were incubated in complete medium under normoxic conditions for 30 hours. Data are expressed as the mean±SEM of 6 independent experiments. * $P<0.01$ vs. control (COM); †$P<0.01$ vs. 0 μM CORM-3[24]

In an oxidative damage protection test, paraquat was used, a superoxide anion generator to promote oxidative stress. Figure 6B shows the cell viability

with varying concentration of paraquats treated with various concentration of CORM-3. All of the CORM-3 containing samples show significant improvement in cell viability compared to the control group. Similar to the previous studies, 25 μM of CORM-3 showed the most effective protection.

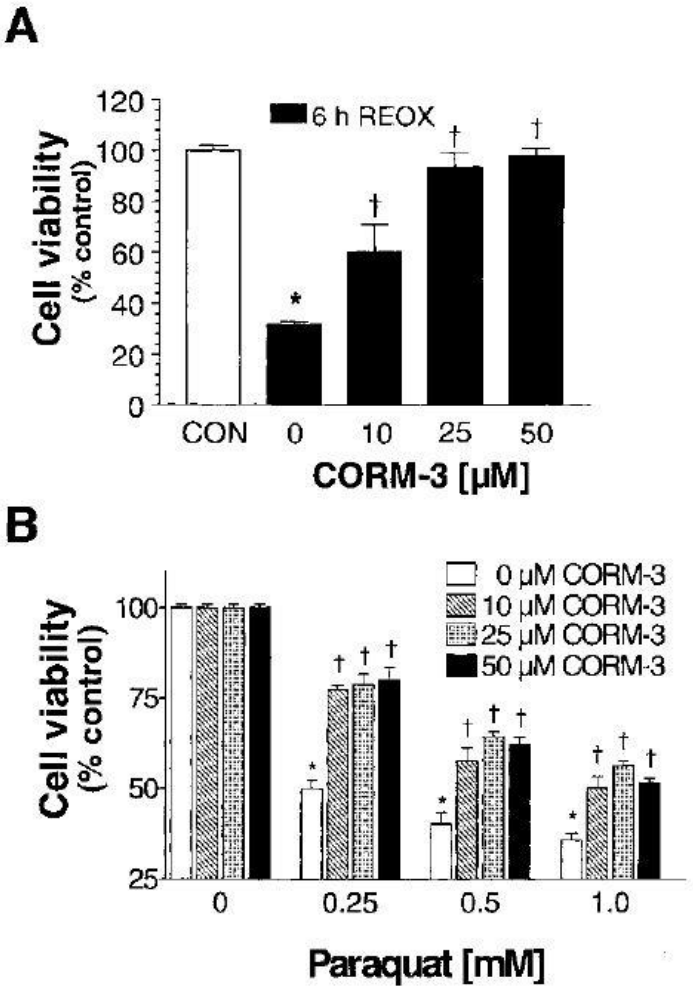

Figure 6. Protective effects of CORM-3 against oxidative stress. A: same condition as in Figure 5, but CORM-3 is introduced during reoxygenation phase. B: Cells were exposed to increasing concentrations of paraquat (0.25 to 1 mmol/L) in the presence or absence of CORM-3 and cell viability determined after 24 hour incubation. Data expressed as the mean±SEM of 6 independent experiments. * $P<0.01$ vs. control (COM); †$P<0.01$ vs. 0 μM CORM-3[24]

The next aspect of CO Clark *et at.* tested was the cardioprotective effects against myocardial ischemia-reperfusion injury. In this experiment, isolated rat hearts underwent 30 minutes of ischemia, then reperfused for 60 minutes. During the process, they measured left ventricular developed pressure (LVDP), maximal contraction, and relaxation pressures (Figure 7). It is clear to see that only the group treated with CORM-3 showed an inotropic effect, or strengthening of the muscular contraction. Also, intracranial epidural pressure (EDP) and the cerevral perfusion pressure (CCP) were examined as they are typically of post ischemic myocardial dysfunction. As shown in Figure 8, the group with CORM-3 showed minimal EDP and CCP present in the system, implying that there would be little to no post ischemic myocardial dysfunction.

Lastly, the studies on prevention of cardiac allograft rejection in mice was conducted. The control group of CBA mice with BALB/c hearts transplanted was treated with saline. All organs stopped beating within 9 days of transplantation. When treated with CORM-3, the survival time of hearts transplanted were extended to 18 days. At 25 days, 60% of the cells were still viable, and at 30 days, 40% (Figure 9).

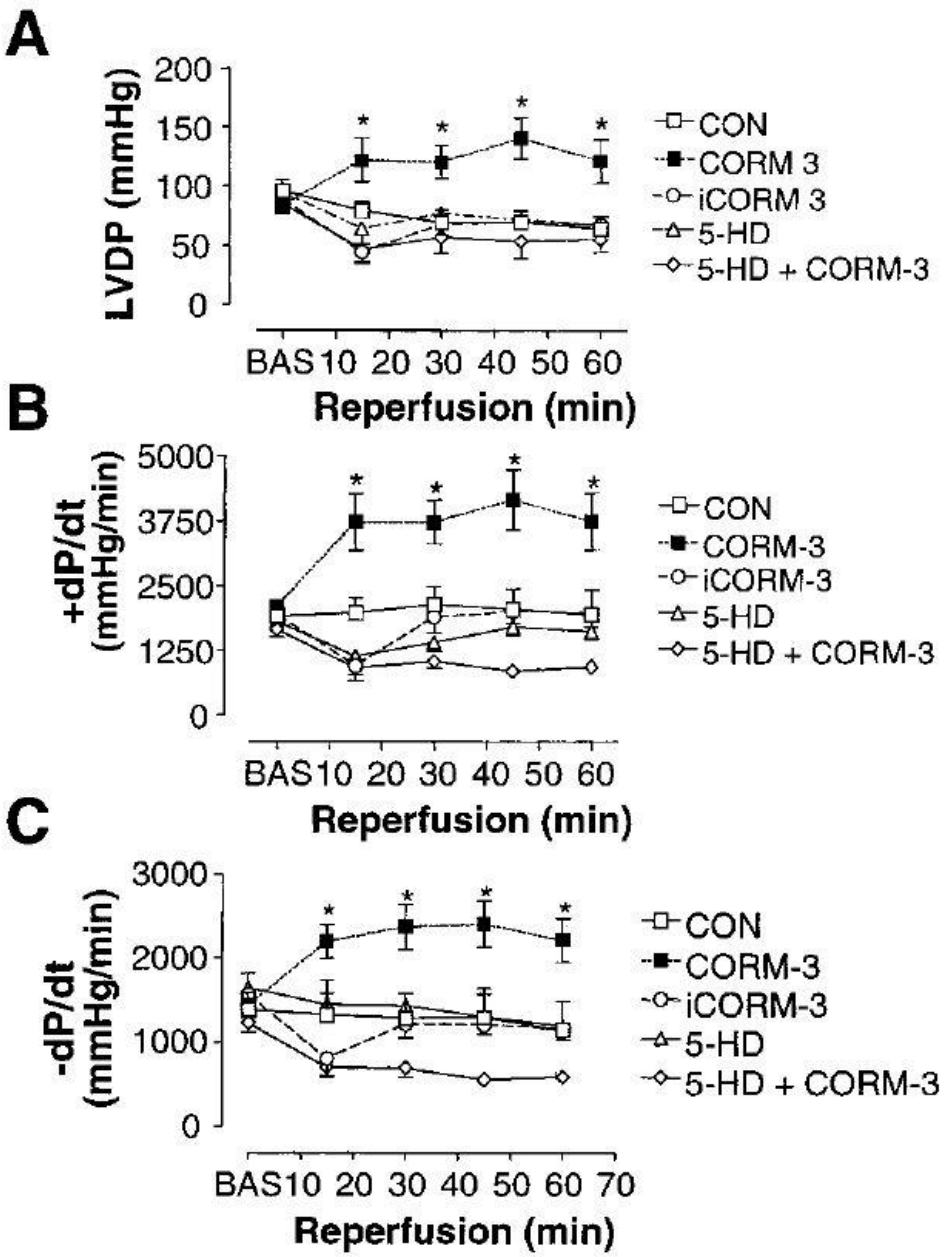

Figure 7. Preservation of myocardial contractility by CORM-3 after ischemia-reperfusion. Isolated rate hearts were subjected to 30 minutes of global ischemia and then reperfused for 60 minutes in the absence (CON) or presence of CORM-3 (10 μM), iCORM-3 (10 μM), 5-HD (50 μM), or a combination of CORM-3 plus 5-HD. Left ventricular developed pressure (LVDP; A), maxima contraction (+dP/dt; B), and relaxation (-dP/dt; C) were continuously recorded during the reperfusion phase.

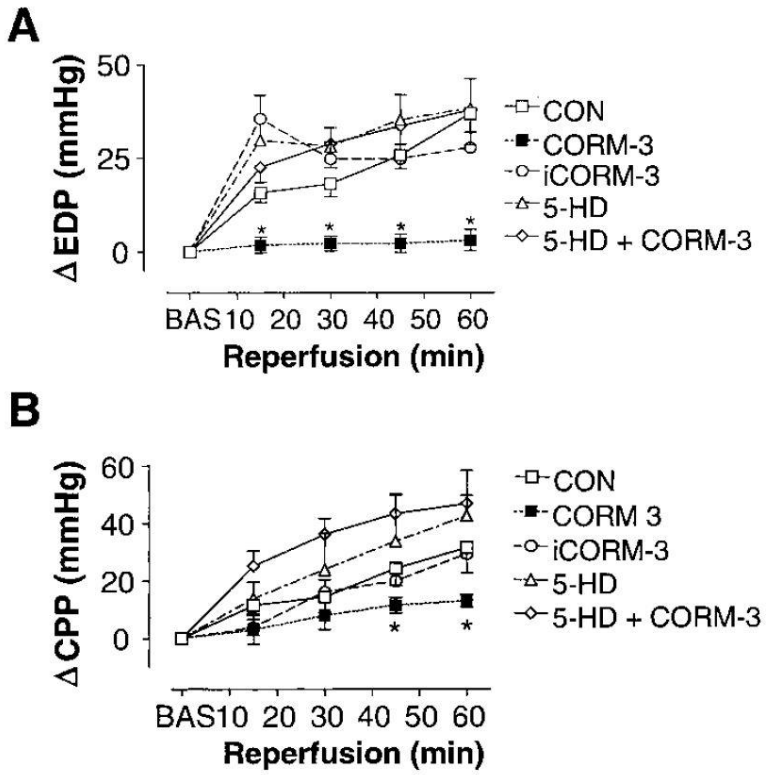

Figure 8. Preservation of coronary and end-diastolic pressure by CORM-3 after myocardial ischemia-reperfusion.

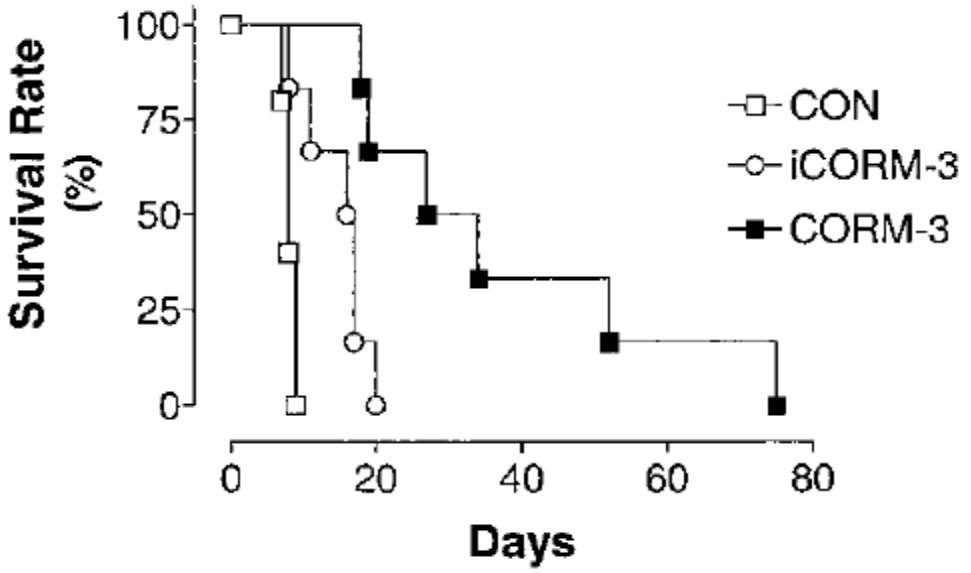

Figure 9. CORM-3 protects against ardiac allograft rejection. Hearts from BALB/c mice were transplanted into CBA mice after treatment with saline (control), CORM-3 (40 mg/kg), or iCORM-3 (40 mg/kg). and the survival rate assessed.

3.2 PHOTOACTIVE MANGANESE CARBONYL CORM

In 2012, Gonzalez *et al.*[25] reported a series of manganese based CORMs. While CORM-3 relies on a change in pH to release CO, their CORMs used the photodissociation property of the metal carbonyl. The photoactive manganese carbonyls were synthesized with different tridentate ligands with varying degrees of conjugation in their frameworks, which adjusted the properties such as solubility and electronic absorption. Among the reported CORMs, $[Mn(pqa)(CO)_3]ClO_4$ (Mn-pqa, pqa = (2-pyridylmethyl)(2-quinolylmethyl)amine) showed the most promising results in biological applications, which we later adopted in our research presented in Chapter 5.

Figure 10 compares the electronic absorption spectra of the three different Mn carbonyls; $[Mn(tpa)(CO)_3]ClO_4$ (Mn-tpa, tpa = tris(2-pyridyl)amine), $[Mn(dpa)(CO)_3]Br$ (Mn-dpa, dpa = N,N-bis(2-pyridylmethyl)amine), and Mn-pqa. There are two aspects where Mn-pqa shows advantage over the other two. First, its absorption peak is more red-shifted. It is a well-known fact that intense UV light can damage the skin. If these compounds were to be photoactivated under the skin or within the cells, a stronger UV light source would be needed to penetrate into the cell. This would cause damage to the surrounding cells, which defeats the purpose. Although all of the compounds are selective to UV light, Mn-pqa shows the most red-shifted electronic absorption peak, which makes it the safest choice in biological use. It also shows the strongest absorption among the three.

Another advantage of Mn-pqa over the other two is its stability in aqueous buffer. While Mn-tpa and Mn-dpa lost a small portion of CO (over h) in tissue

bath media, Mn-pqa did not show any loss of CO in the dark. Although the rate of CO liberation was slower than in MeCN, Mn-pqa showed an excellent capacity of CO delivery in PSB.

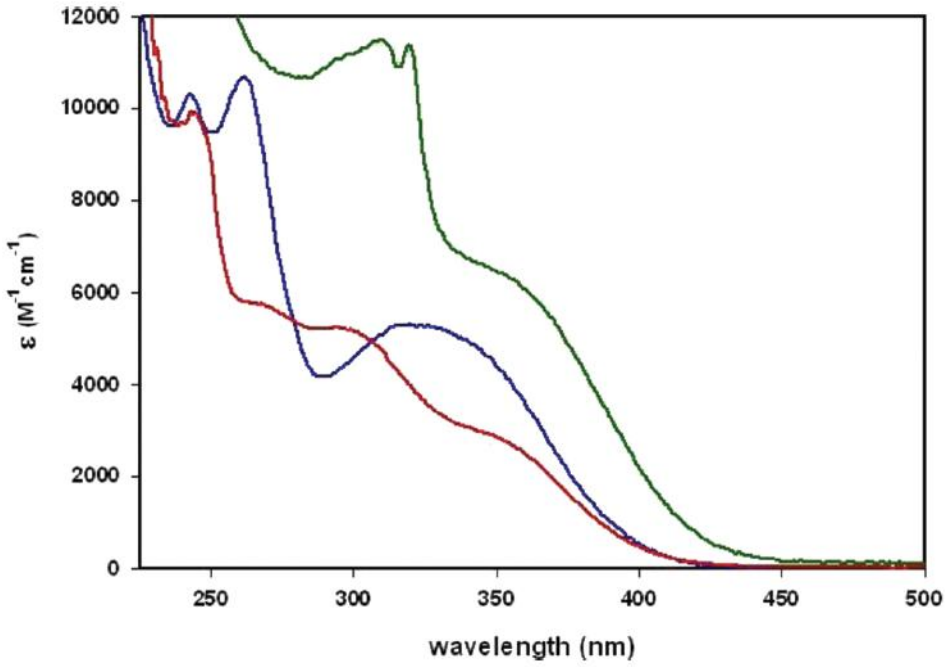

Figure 10. Electronic absorption spectra of [Mn(pta)CO_3]ClO4 (blue trace) [Mn(dpa)$(CO)_3$]Br (red trace), and [Mn(tpa)$(CO)_3$]ClO_4 (green trace) in MeCN.

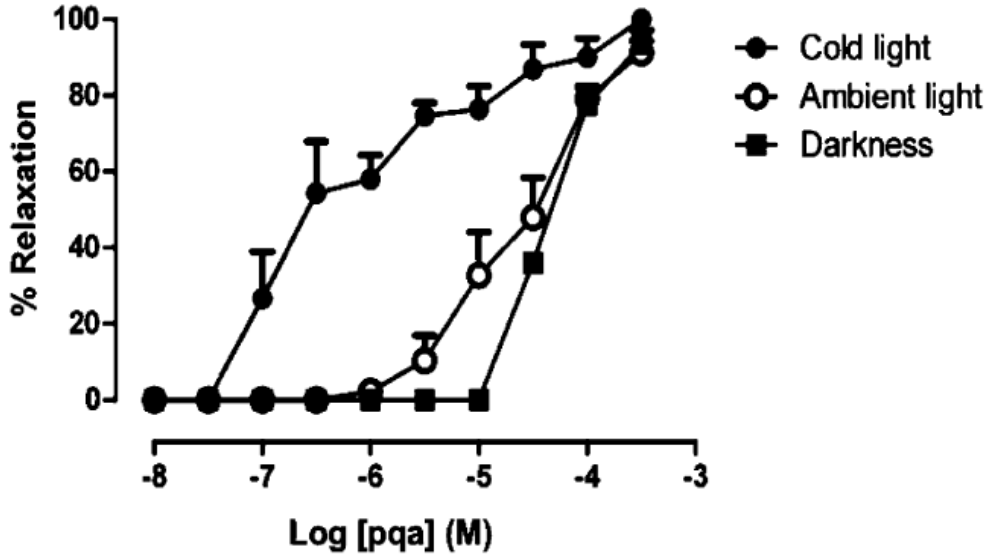

Figure 11. Vasorelaxation of mouse aorta muscle rings by Mn-pqa upon exposure to visible (cold) light and ambient room light.

Figure 11 shows the result of vasorelaxation studies. While in ambient light and darkness, no significant relaxation was observed. However, with visible cold light exposure, rapid muscle relaxation is evident.

CHAPTER 4

THE ENCAPSULATION MATERIALS

One of the biggest issues in the area of pharmaceutical drugs is poor solubility. This causes irregular and delayed absorption and makes it difficult to control the dosage, reducing overall efficacy of the drug. As a solution, drug delivering materials (DDM) were developed. Pharmaceutical drug carriers or drug encapsulation materials are expected to have several characteristics: 1) biocompatibility, 2) easy and reasonably low expense to prepare, 3) to be able to modify textural and surface properties, 4) to possess a high loading capacity, and 5) to specifically or nonspecifically accumulate in required sites in the body.[26] In this chapter, some of the important aspects of the encapsulation materials will be discussed. Also MCM-41, the parent type of DDM used for our research, will be discussed separately.

4.1 BIOCOMPATIBILITY

When a DDM is introduced inside the body, it is expected to withstand the physiological environment and have no side effects such as toxic, carcinogenic, immunogenic, and inflammatory responses. Since the purpose of using a drug delivery material is to be able to administrate the drug application area and time, long-term biocompatibility is an important issue. This aspect is a two-step process that involves the time-dependent effects of the host on the material and of the material on the host.[27] In order words, for a desired length of the time, the DDM

should stay stable as well as exist as the loaded drug. Some of the factors that determine this biocompatibility are the shape and size of the material, as well as its surface chemistry.[27]

Depending on the route of drug administration, specific textural and surface properties of the DDM can be adjusted in order to deliver drugs that would not be possible if directly used. For a systemic route of administration, drugs are given to the a patient non-locally such as into a vein or bone marrow. Since it is injected into an aqueous environment, the drug has to be hydrophilic in order to be effective. This becomes a huge disadvantage because not all drugs can be modified to be hydrophilic. For example, the anticancer drug camptothecine (CPT) and its derivatives are very effective against many different carcinomas, but could not be used in clinical application due to the poor water solubility of the drug.[28]

In order to overcome this disadvantage, there is a reported case where a DDM was used to deliver CPT by Tamanoi and co-workers. For DDM, they used mesoporous silica nanoparticles (MSN) which provided high loading capability for hydrophobic drugs and stability in aqueous media. They modified the surface of the nanoparticles with trihydroxysilylpropyl methylphosphonate (THMP) after particle formation in order to reduce the aggregation and increase the stability of the particles in aqueous solution (Figure 12). They also confirm the successful cell uptake by functionalizing the surface of the particles with fluorescein isothiocynate (FCTC) so that the particles in the cells are observable with fluorescence and confocal microscopy. The image of the cells with uptaken nanoparticles are shown in Figure 13.

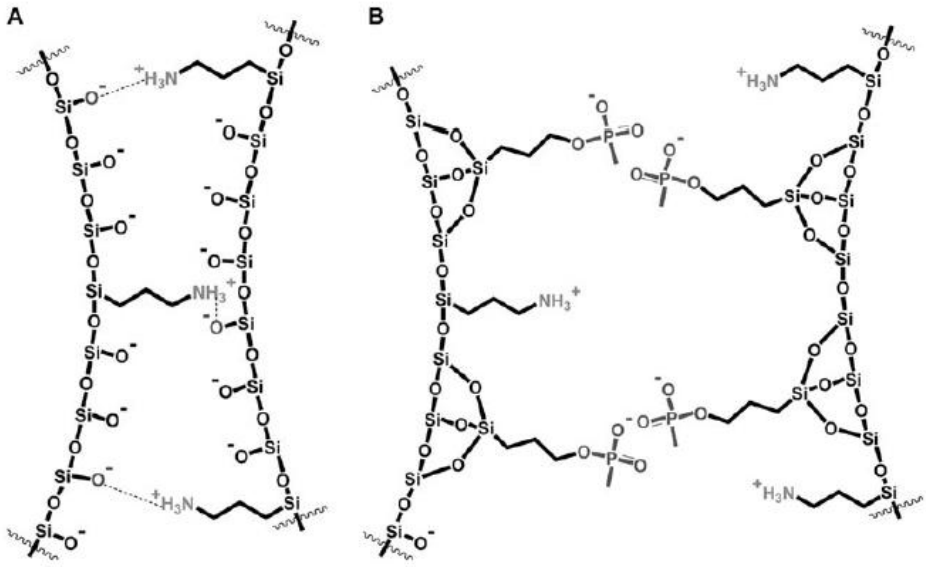

Figure 12. A) Aggregation between the nanoparticles was caused by the interparticle hydrogen bonding between the surface silanol groups and the ammonium groups. b) Surface modification with THMP increased the electrostatic repulsion between the nanoparticles and decreased the aggregation.

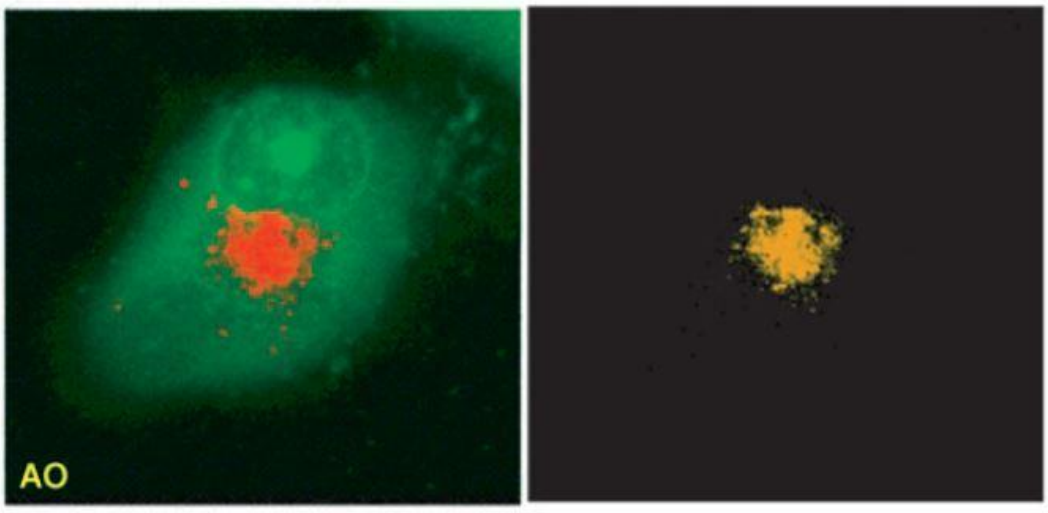

Figure 13. Uptake of the nanoparticles by cancer cells. PANC-1 cells stained with Acridine Orange (AO, left) and the fluorescence of the nanoparticles within the same cell (right).

Use of DDM is also applicable in the topical route of drug administration. One of the good examples is the treatment of osteomyelitis. In a paper published in 1993, they used bioerodible polymers as the drug delivery system. This method

was attempted in order to overcome drawbacks of the previous methods of treatments: use of systemic antibiotics, the local implantation of non-degradable drug carriers, and surgical debridement. When antibiotics are given systemically, it risks various organs due to its toxicity and also takes many weeks to effect a cure. Use of non-degradable drug carriers such as *para*-methoxy-*N*-methylamphetamine (PMMA) has shown efficacy, but the material must be removed in a second surgical procedure several weeks after implantation. Using bioerodible polymeric system improves these aspects of the previous drug delivery system as it avoids the need for the secondary surgery to remove the used material.

In a review by Arcos *et al*., there is an interesting note on an aspect of implementation of DDM.[27] When the DDM is introduced into the blood, certain proteins are rapidly adsorbed onto the surface of the material followed by platelet adhesion. Then immune and inflammatory cells form a fibrous capsule around the material as a natural response which does not depend on its biocompatibility. However, that collagen capsule does reduce its efficiency as an DDM. Almost all biomaterials are known to cause surface-induced thrombosis, which, besides the medical complications related to thrombi, affects the drug-release profile. Thus, the longer DDM stays within the system, overall efficacy decreases.

4.2 TEXTURAL PROPERTIES OF DDM

There are quite a few aspects of DDM that can be modified in order to tune its performance such as pore size, pore volume, particle shape, particle size,

or surface properties. While each component serves a different role in the drug delivering process, this section will focus on the pore size and the particle size.

4.2.1 PORE SIZE

While there are DDMs that carry the cargo compounds in a hollow space of a particle[29-31]or attached on the surface[32], typically they are composed of a matrix of channels, or mesopores. Having a mesoporous structure increases the surface area and the pore volume as well as control the size of the guest molecule by adjusting the size.

A common method of loading the cargo compounds into DDMs is diffusion. In a typical procedure, one would soak the empty DDMs in a highly concentrated drug solution for a set period of time in order to load them. For that reason, the size of the pore should be big enough for the drug compounds to diffuse inside the channels. It is reported that the change in pore size can influence the loading kinetic process.[33] Figure 14 shows their investigation on comparing the loading kinetics into mesoporous silica as a function of time. For MCM-41 groups, the numbers of the carbons of the template are denoted with subscript. The pore size of MCM-41_{12} here is 2.01 nm and for MCM-41_{16}, 2.17 nm. It is evident that the one with larger pore size has achieved faster loading. In the case of SBA-15, despite having a much bigger pore size (9.37 nm), the size of the particle was much smaller then MCM-41_{16}, which resulted in a decrease of the loading kinetics.

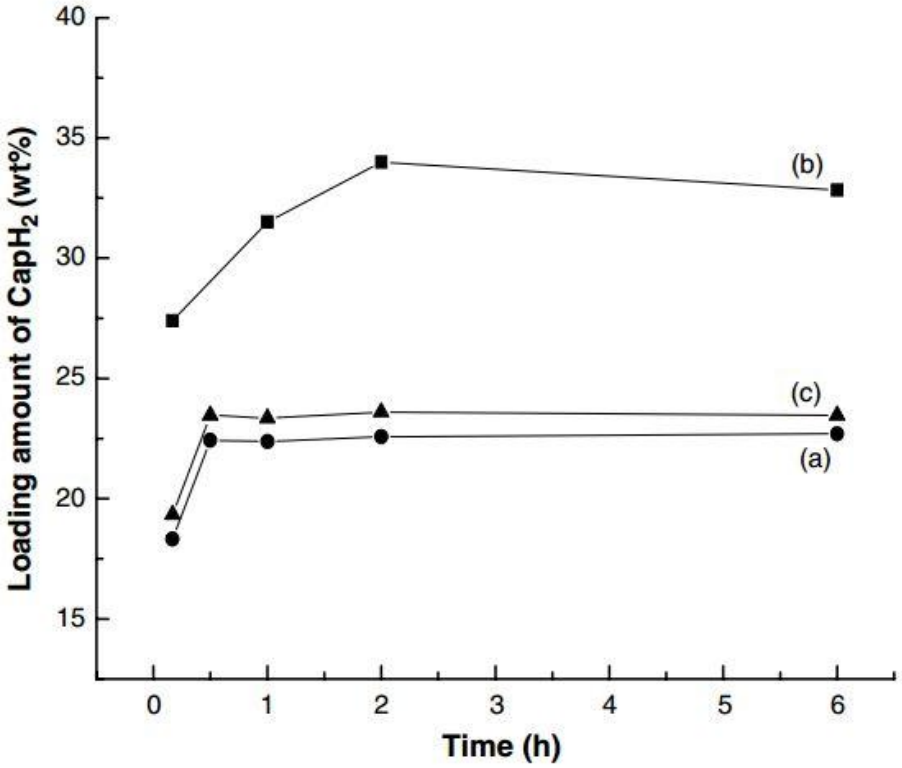

Figure 14. The loading amount of CapH2 in different mesoporous silica samples (a) SBA-15 (circle symbols), (b) MCM-41_{16} (square symbols), (c) MCM-41_{12} (triangle symbols) as a function of time.

By the same principle, pore size influences the kinetics of releasing the guest molecule, which is the more crucial aspect in application.[34] Figure 15 shows the studies on the kinetics of ibuprofen liberation to SBF solution. The pore diameters of the MCM-41s are as follows: MCM-41_{16} (3.6 nm); MCM-41_{12} (3.3 nm); MCM-$41_{8(70\%\text{-}10(30\%)}$ (2.7 nm); and MCM-$41_{8(85\%)\text{-}10(15\%)}$ (2.5 nm). It is very evident that the rate of release is higher as the pore size increases. They also report that between the pore sizes 2.4 nm and 3.6 nm, the rate difference is as large as a factor of five (24 mg/h for 3.6 nm and 5 mg/h for 2.5 nm). Although the difference in release rate would vary with the material of DDM and the guest molecule, the fact that bigger pore size leads to a higher release rate still stands.

With bigger pore size, there is more room for the solvent to diffuse into the channel and the counter-diffusion of the guest molecule out of the channels should be easier. Thus, it should be possible to adjust the amount of guest molecule release by adjusting the pore size of DDM.

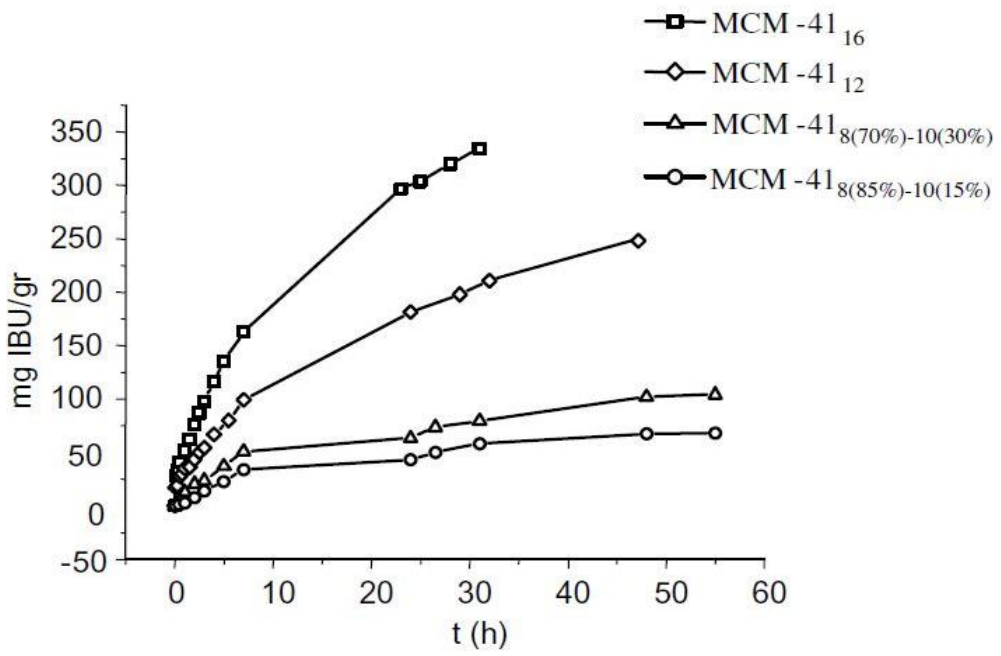

Figure 15. Ibuprofen delivery from different pore sized MCM-41.

4.2.2 PARTICLE SIZE

Particle size is an important parameter in designing suitable cell-tracking and drug-carrier nanoparticle systems, because it determines the mechanism and rate of cell uptake of a nanoparticle and its ability to permeate through tissue.[35]

In 2009, Mou *et al*. reported the study of the influence of particle size on the cell uptake performance. They have synthesized several different sizes of dye-

functionalized(fluorescein isothiocyanate, FITC) MSN particles (FITC-MSN) and cultured it with HeLa cells for 5 hours, followed by ICP-MS to detect the silicon concentration. Figure 16 shows a clear difference for each size. They have concluded that a particle size of 50 nm is the optimum size for cell uptake, and mentioned some other reports agreeing with their data.[36-38] A report from Chan *et al*. also studied the cellular uptake kinetics of gold nanoparticles with different sizes. Interestingly, it showed the same trend as the cell uptake capacity (Figure 17, Figure 18), which leads to a conclusion that a 50 nm particle size is favored not only in uptake capacity, but kinetically as well. Also, Chan's study was perofrmed with gold nanoparticles instead of MSN, which suggests that the influence of particle size on cell uptake is independent of the DDM composition.

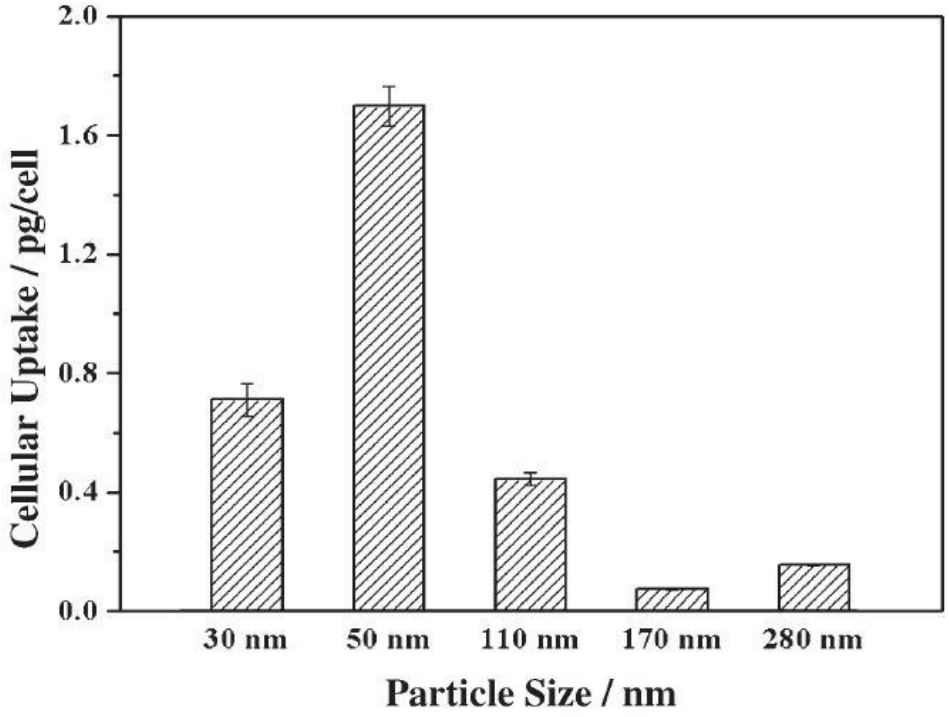

Figure 16. Cell uptake of FiTC-MSN-x. The graph shows the mass of silicon per cell versus size of FITC-MSN-X.

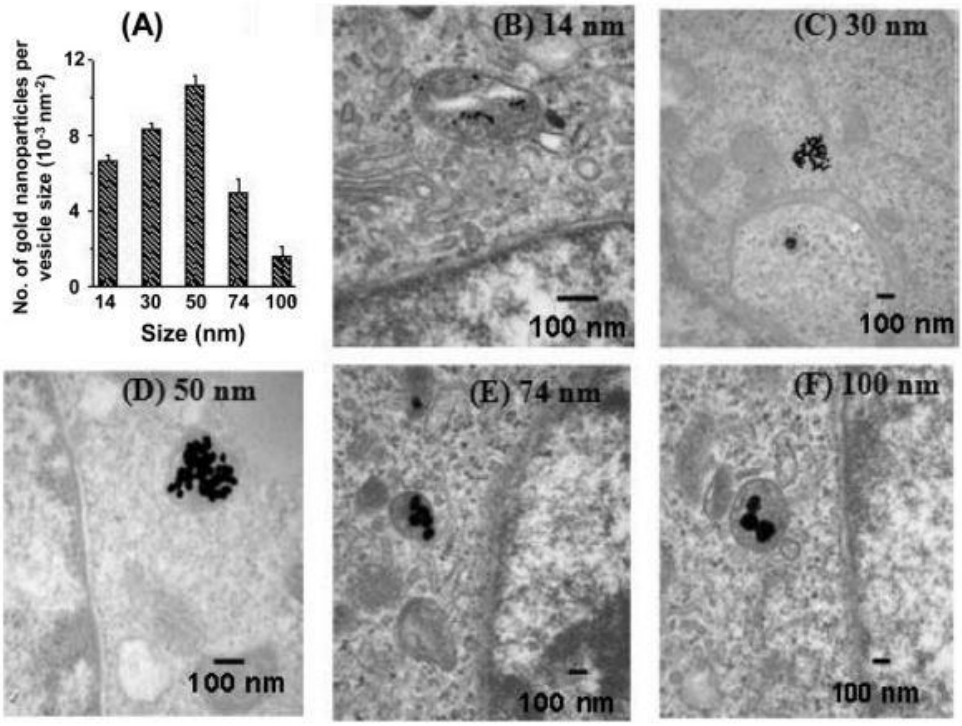

Figure 17. Transmission electron microscopy imaging and measurements of gold nanoparticles in cells. (A) The graph of number of gold nanoparticles per vesicle diameter vs. nanoparticle size. (B-F) TEM images of gold nanoparticles with sizes 14, 30, 50, 74, and 100 nm trapped inside vesicles of HeLa cell, respectively. (cite)

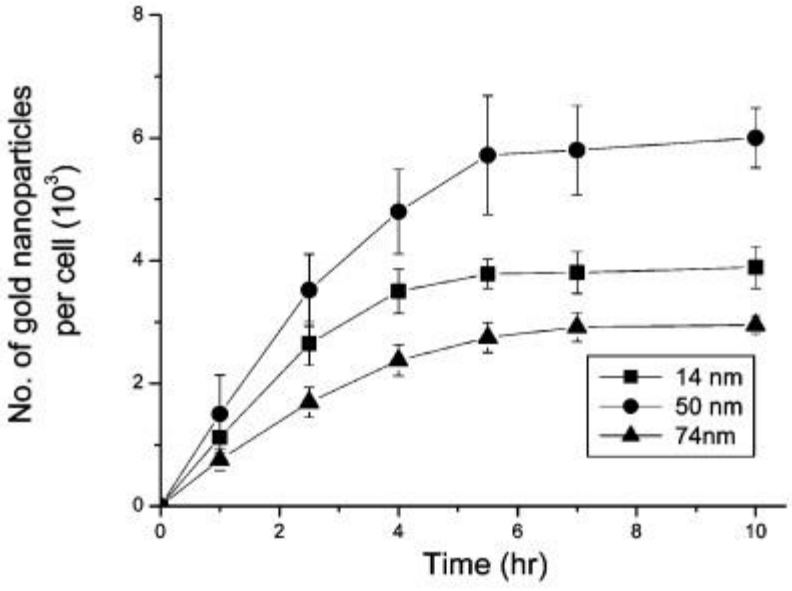

Figure 18. Cellular uptake kinetics of gold nanoparticles. Cellular uptake of gold nanoparticles as a function of incubation time for three different size gold nanoparticles (nanoparticle diameters 14, 50, and 74 cm).

4.3 MCM-41

MCM-41 (Mobile Crystalline Material, structure no. 41) is a mesoporous silicate material that was developed in 1992 by Mobil Research and Development Corporation.[39] It is a member of M41S which exhibits a hexagonal arrangement of mesopores that are adjustable with different conditions in the synthesis. In 2001, it was first introduced as a drug delivery material by Pérez-Pariente *et al*.[40] Since then, MCM-41 type of drug delivery system have become very popular for several reasons: 1) Uniform mesoporous structure; 2) Ease in modification; and 3) biocompatibility. In this chapter, we will discuss its synthetic aspects, including mechanism of formation and shape determining factors.

In a typical synthesis of MCM-41, there are three main chemical components: silicate source, organic surfactant, and base catalyst. Each components plays a critical role in shape determination which will be discussed in 4.3.1.

According to the proposed mechanism for the formation of MCM-41, it starts with surfactants forming micellar rods. Then those form a hexagonal array which becomes a template for silicate. After the complete formation of the silicate structure around the hexagonal array, the product is filtered then calcined at high temperature to burn out the surfactant, leaving only the silicate structure (Figure 19). In a report by Cui *et al*., they proposed a similar mechanism of MCM-41 formation. However, in their proposal, the silicate source binds to the surfactant by ion-exchange before the formation of micellar matrix (Figure 20).[14] A schematic representation of both proposals is shown in Figure 21 for comparison.

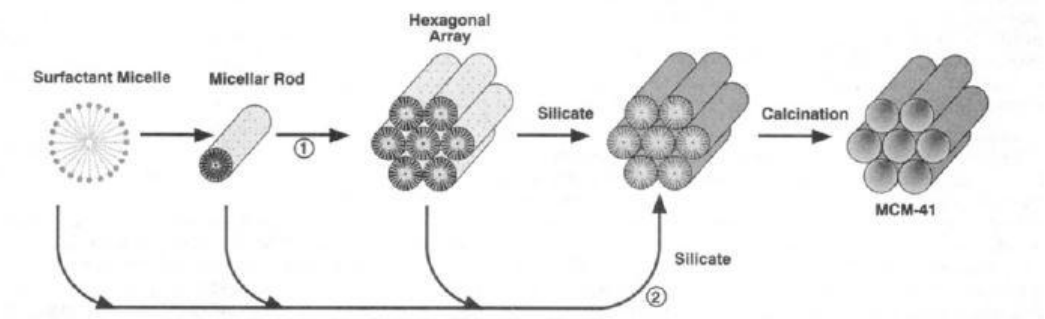

Figure 19. Possible mechanistic pathways for the formation of MCM-41: (1) liquid crystal phase initiated and (2) silicate anion initiated.

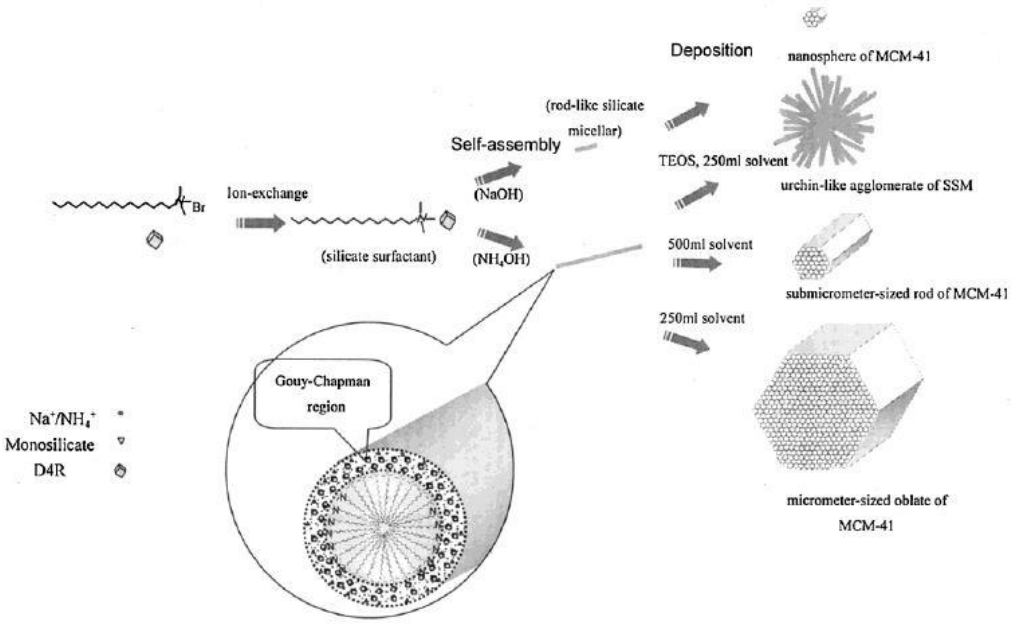

Figure 20. Schematic illustration for morphogenesis mechanism of MCM-41.

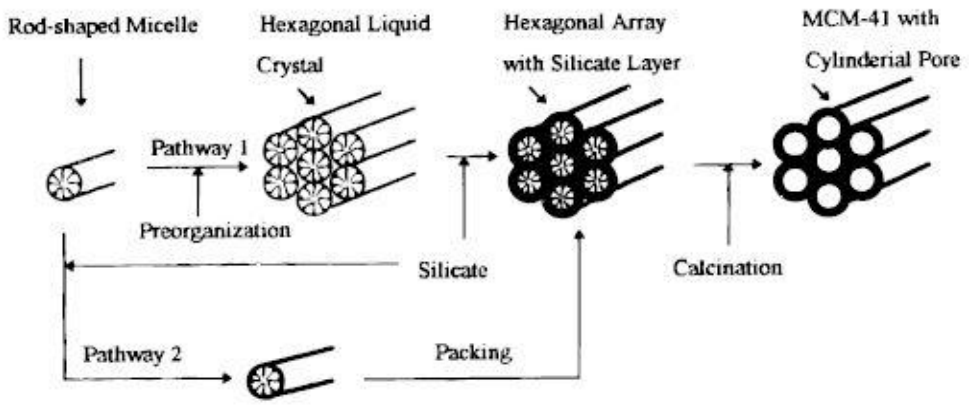

Figure 21. Schematic illustrations for both proposed mechanisms (Figure 19 and Figure 20) of MCM-41 formation.[42]

4.3.1 SHAPE DETERMINING FACTORS

According to Cai *et al*.,[41] the factors determining the micelle formation are the concentration of tetraethyl orthosilicate (TEOS) and hexadecyltrimethylammonium bromide, (CTAB). When the concentration of TEOS is greatly reduced, urchin like agglomerates is formed as in Figure 20. A low concentration of CTAB results in a low concentration of self-assembled silicate micelles (SSMs), leading to the formation of rod-like submicrometer particles of MCM-41.[41]

CTAB, the surfactant in MCM-41 synthesis, has shown a greater role than shape determination. As discussed in earlier section, it is possible to adjust the pore size of the MCM-41 by changing the length of the hydrocarbon of the surfactant. When Horcajada *et al*.[34] studied the influence of pore size of MCM-41 matrices on drug delivery rate, they synthesized different pore size by using different types of surfactant. For smaller ones, they used octyltrimethylammonium bromide (C8TMAB, C8) and for larger size, decyltrimethylammonium bromide (C10TMAB, C10) was used. The only difference between two are the length of the hydrocarbon chain, which is reflected on the size of the pore.

Another main chemical component is the base catalyst. Cai *et al*. reported that NaOH favors shorter micelles while NH_4OH longer micelles. The length of the micelles determine the size of the MCM-41 particle size. This report corresponded with my own data as well. Although it was not the final condition of the MCM-41 used for my research, I was able to observe the size difference from using NaOH and NH_4OH (Figure 22). Although the particle sizes were not

uniform, it is still easy to conclude that the particles using NH_4OH (Figure 22a) were bigger particle size on average than those with NaOH. (Figure 22b).

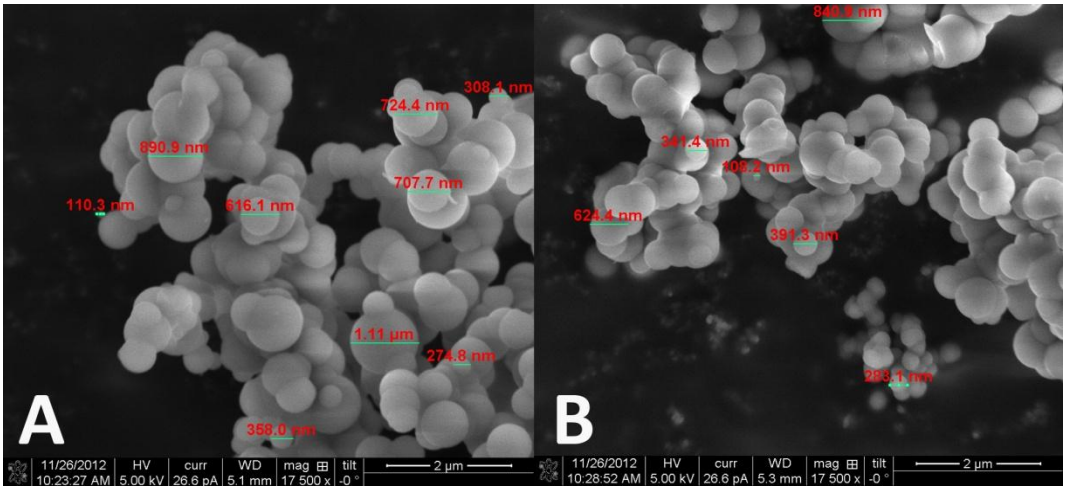

Figure 22. Comparison of MCM-41 particle size with different base catalyst. A) NH_4OH; B) NaOH.

While trying to optimize the MCM-41 particles, there were some other factors discovered that influenced particle size and shape. One of them is the steering speed in preparation. In a typical procedure, once everything is mixed, the solution is stirred for a certain amount of time. In this step, faster stirring speed resulted in smaller, more monodisperse particles. In Figure 23, two samples were synthesized in the same condition except the stirring speed, one (left) at 250 rpm and the other (right) at 625 rpm. The one with 250 rpm shows some oversized particles in the corner while the other one does not show significant size variation. This result seems to be related to the kinetics of the self-assembly of micellar rods. With faster stirring speed, the micellar rods would be dispersed through the solution more evenly, leading to monodisperse particle formation. However as the micelles are moving faster in the solution, it would make self-assembly harder, causing smaller particle size over a given time.

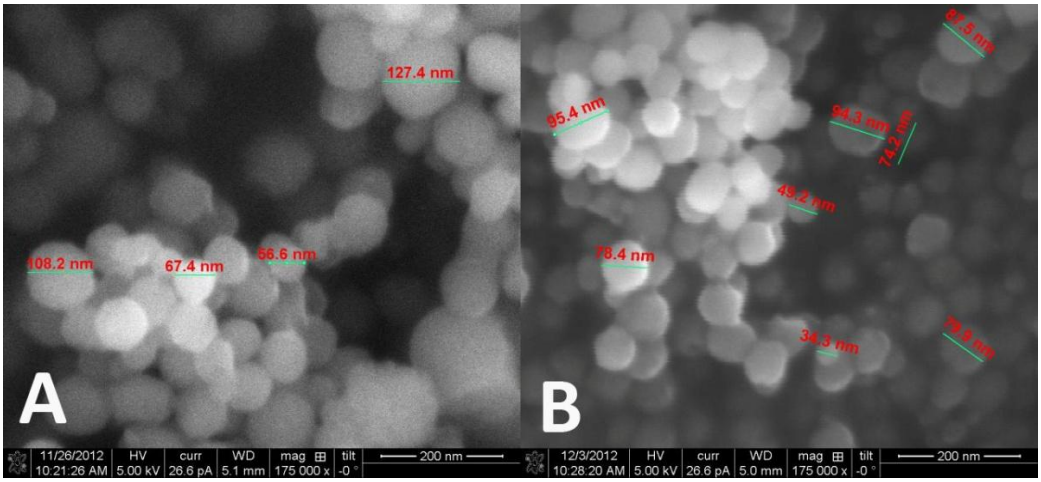

Figure 23. Two samples of MCM-41(Si/Al = 1:20) prepared with different stirring speed: A) at 250 rpm; B) at 625 rpm.

Doping with aluminum also showed alteration in the shape. In Figure 24, the two samples were prepared with the same condition as above, but with 4 times higher aluminum content (Si/Al = 1:5). The shape of the particle changed to a short rod (right), and with slower steering speed, the particle grew longer (left).

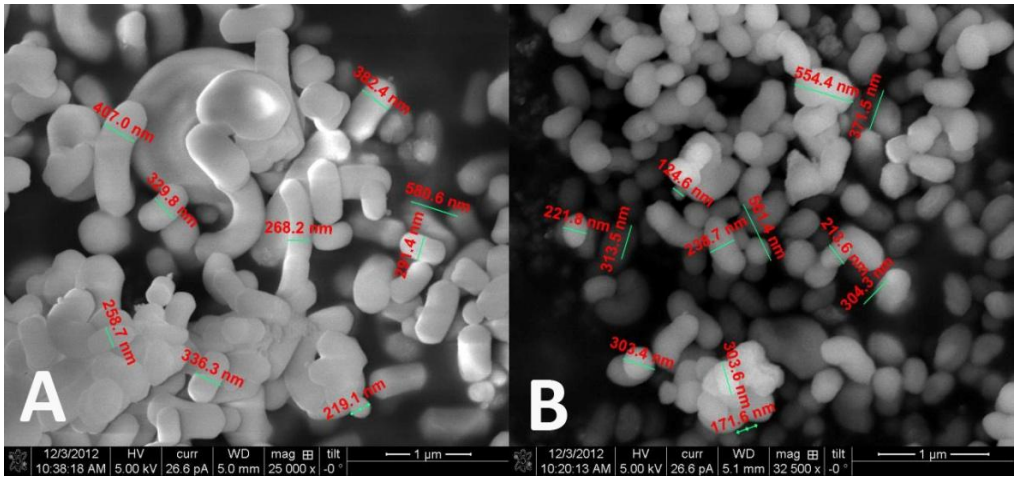

Figure 24. Two samples of MCM-41 with higher aluminum content (4 times more than Figure 23, Si/Al = 1:5) prepared with different steering speed: A) at 250 rpm; B) at 625 rpm.

CHAPTER 5

CORMs IN SPHERICAL MCM-41

In this chapter, both experimental methods and data of our research are discussed in detail.

5.1 MATERIALS AND EXPERIMENTAL

MATERIALS

For Al-MCM-41 synthesis, n-hexadecyltrimetilammonium bromide (C_{16}TMABr) was purchased from Aldrich Chemical Co and used without further purification. Tetraethyl orthosilicate was purchased from Acros Organics and sodium aluminate ($NaAlO_2$) from Strem Chemicals. Both were used as received.

For $Mn(pqa)(CO)_3]ClO_4$, manganese pentacarbonyl bromide {$[Mn(CO)_5Br]$} was purchased from Alfa Aesar. The ligand (2-pyridylmethyl)(2-quinolylmethyl)amine (pqa) and the starting salt fac-$[Mn\text{-}(CO)_3(MeCN)_3](ClO_4)$ were synthesized following published procedures.[25] Solvents were purified and/or dried by standard techniques prior to being used.

Synthesis of Spherical Al-MCM-41 (MSN)

It is reported that the negatively charged aluminum sites of Al-MCM-41 improves the loading through an ion-exchange mechanism.[43] The cations

exchange for the Na^+ ions inside the host, and hence the extent of loading is facilitated by a combination of ion exchange and passive diffusion. Thus, mesoporous silicate for this project began with Al-MCM-41 and did not compare loading capacity with pure silicon MSN. The aluminum content of the nanoparticle was set to be 5%, as more than 5% aluminum content distorted the shape of the sphere. More on this topic was discussed in Chapter 4.

Mesoporous supports were synthesized in their spherical shape by modifying the procedure reported by Ca *et al*[41]. 3.5 mL of NaOH (2 M) solution was mixed with 480 mL of distilled water. 1.0 g of C_{16}TMABr was added to the solution at 80 ℃ and stirred for 15 minutes at 625 rpm. Under stirring, 0.098 g of $NaAlO_2$ was added[44], then 4.58 g of tetraethylorthosilicate (TEOS) was added drop-wise over two minutes. These amounts gives the molar composition of 1.00 (TEOS) : 0.13 (C_{16}TMABr) : 1197.00 (H_2O) : 0.31 (NaOH) : 0.05 ($NaAlO_2$). After 2 hours, the resultant product was filtered, rinsed with distilled water, dried at 55 ℃ in vacuum, and calcined in air at 823 K for 4 hours with a ramp rate of 1 ℃/min.

Loading of $[Mn(pqa)(CO)_3]ClO_4$] into MSN

A batch of 0.1 g of calcined Al-MCM-41 product was added to 5 mL of dichloromethane (DCM) in a 50 mL Schlenk flask containing a magnetic stir bar. The mixture was degassed by three cycles of freeze-pump-thaw. At the end of the last cycle, a batch of 0.1 g of $[Mn(pqa)(CO)_3]ClO_4$] was added to the flask under nitrogen. The solution was thawed to room temperature, then stirred for 3 days

with minimum light exposure. The loaded MSN was filtered using a fritted funnel. The light yellow product was rinsed with 3 x 3 mL of DCM. Finally, the product was dried in vacuo.

5.2 CHARACTERIZATION

To investigate the structure and crystallinity of the samples, the powders were analyzed with a X-ray powder diffractometer, XRD (Rigaku SmartLab diffractometer, CuKα radiation (λ = 1.5418 Å)). The sample was scanned from 1.5° to 7° with a step size of 0.02° and a count time of 1 second at each point.

Sample morphology and microstructure were examined by scanning electron microscopy, SEM (FEI Quanta 3D FEG dual beam SEM/FIB nanofabrication instrument, UCSC), and transmission electron microscopy, TEM (Philips CM200/FEG, National Center for Electron Microscopy, University of Toronto) For SEM analysis, specimens were prepared by dispersing the as preapared powder in acetonitrile and sonicated for ~20 minutes to completely disperse the particles. Then a drop of the solution was dropped onto a glass slide, followed by drying. The sample was sputtered with gold before SEM imaging. For TEM analysis, the specimens were dispersed in acetonitrile and drop coated onto a copper grid.

Analysis of manganese content of the system was determined by inductively coupled plasma-optical emission spectroscopy, ICP-OES (PerkinElmer Optima 4300 DV ICO-OES). X-ray elemental maps were recorded

(simultaneously) using a Hitachi HD-2000 dedicated stem equipped with an Oxford Inca EDS system.

An acid digestion procedure for ICO-OES was used from the protocol described in the literature.[43,45] Batches of 35 mg of the {Mn-CO}@Al-MCM-41 samples were added to the Teflon liners of autoclave bombs, and to each was added 1 mL of a 1:3 mixture of concentrated HNO_3 and HCl. The samples were then frozen by dipping the vessels in liquid N_2. Once frozen, 0.125 mL of 40% aqueous HF was added, followed by immediately sealing the vessels and allowing to warm to room temperature. Vessels were placed in a 150 ℃ autoclave oven for 4 h, then allowed to cool to room temperature. Once it is safe to open the vessel, 12.5 mg of boric acid was added to each sample solution to complex free F^-. Finally, the samples were diluted to 50 mL using Millipore water containing 1% HCO_3^{2-} and transferred to a polypropylene flask for analysis.

Infrared spectra of the materials (in KBr disks) were recorded on a Perkin-Elmer Spectrum-One FR-IR spectrometer.

5.3 RESULTS

5.3.1 MORPHOLOGY OF AL-MCM-41

The monodisperse spherical morphology of Al-MCM-41 was observed with SEM. In the top image of Figure 25, there are about 70 particles shown, with an average diameter of 58.9 nm. Some distortion of the spherical shape and size variation that was observed are due to sonication during SEM sample preparation.

In that process, some of the particles were chipped and lost its smooth surface morphology.

The spherical shape of the particle is more evident in the TEM image (Figure 26), as it magnifies the particle more than SEM. Also, the hexagonal array of typical MCM-41 microstructure is revealed in the image. As discussed in Chapter 4, there are different ways of the silicate micelles to assemble into MCM-41 particles. The TEM image (Figure 26, top) shows different orientations of the Al-MCM-41 relative to the line of vision. The streak in particle A has that the hexagonal arrays perpendicular to the line of vision. In particle B, the channels are parallel to the line of vision, looking more like a honeycomb and has less streak character. The morphologies of particle A and B are schematically illustrated in bottom image of Figure 26.

The diffractogram of the sample was obtained with XRD. The solid line in Figure 27 shows typical MCM-41 type Bragg peaks, which can be indexed as (100), (110), and (200). This suggests that the sample has long-range order and quasi-crystallinity. The cell unit parameter, a_o, between two adjacent pore centers in MCM-41 is calculated according Qiang Cai (eq. 1)[41]

$$a_o = \left(\frac{2}{\sqrt{3}}\right) d_{100} \qquad (1)$$

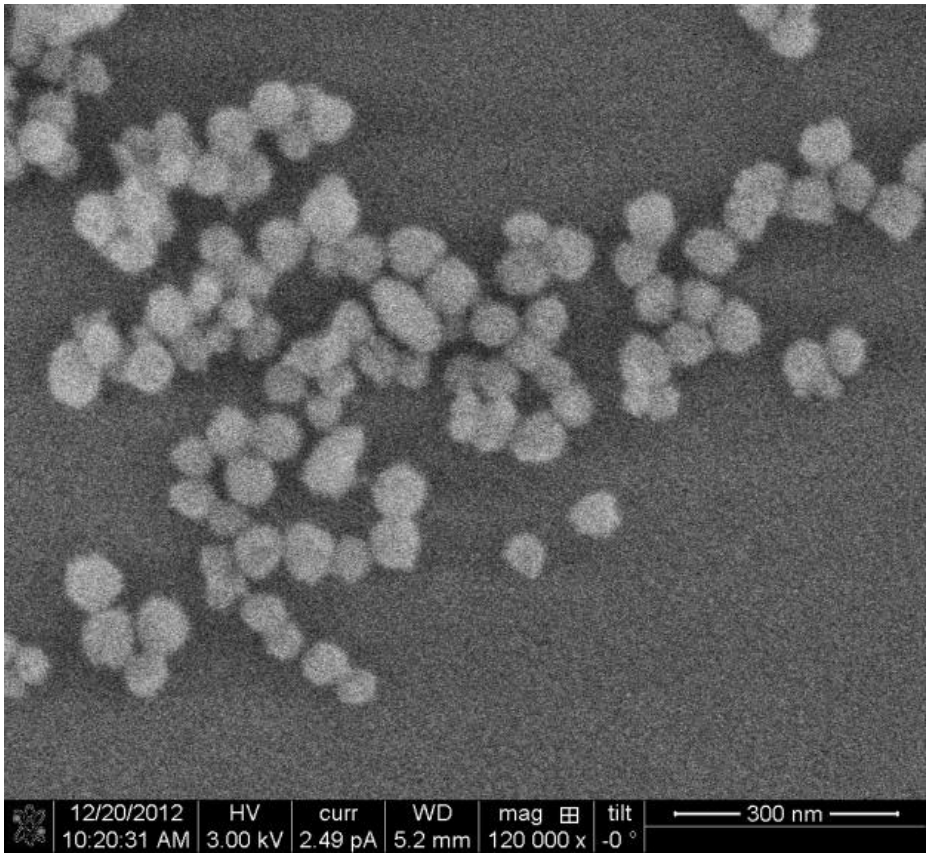

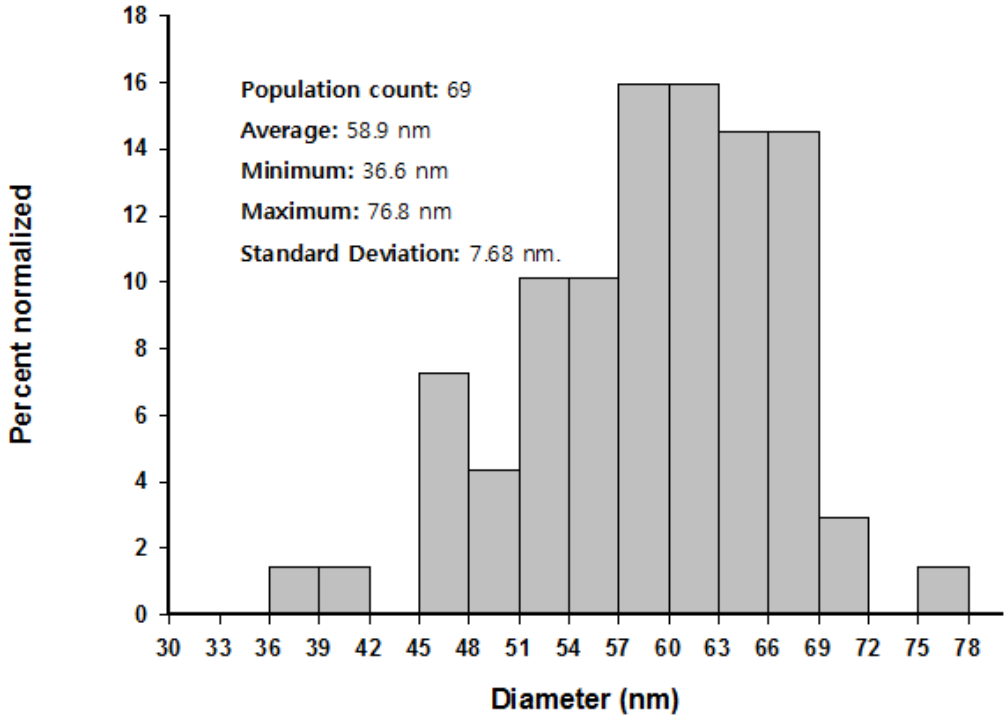

Figure 25. Top: SEM image of calcined Al-MCM-41; Bottom: particle size distribution histogram obtained from the SEM image on top.

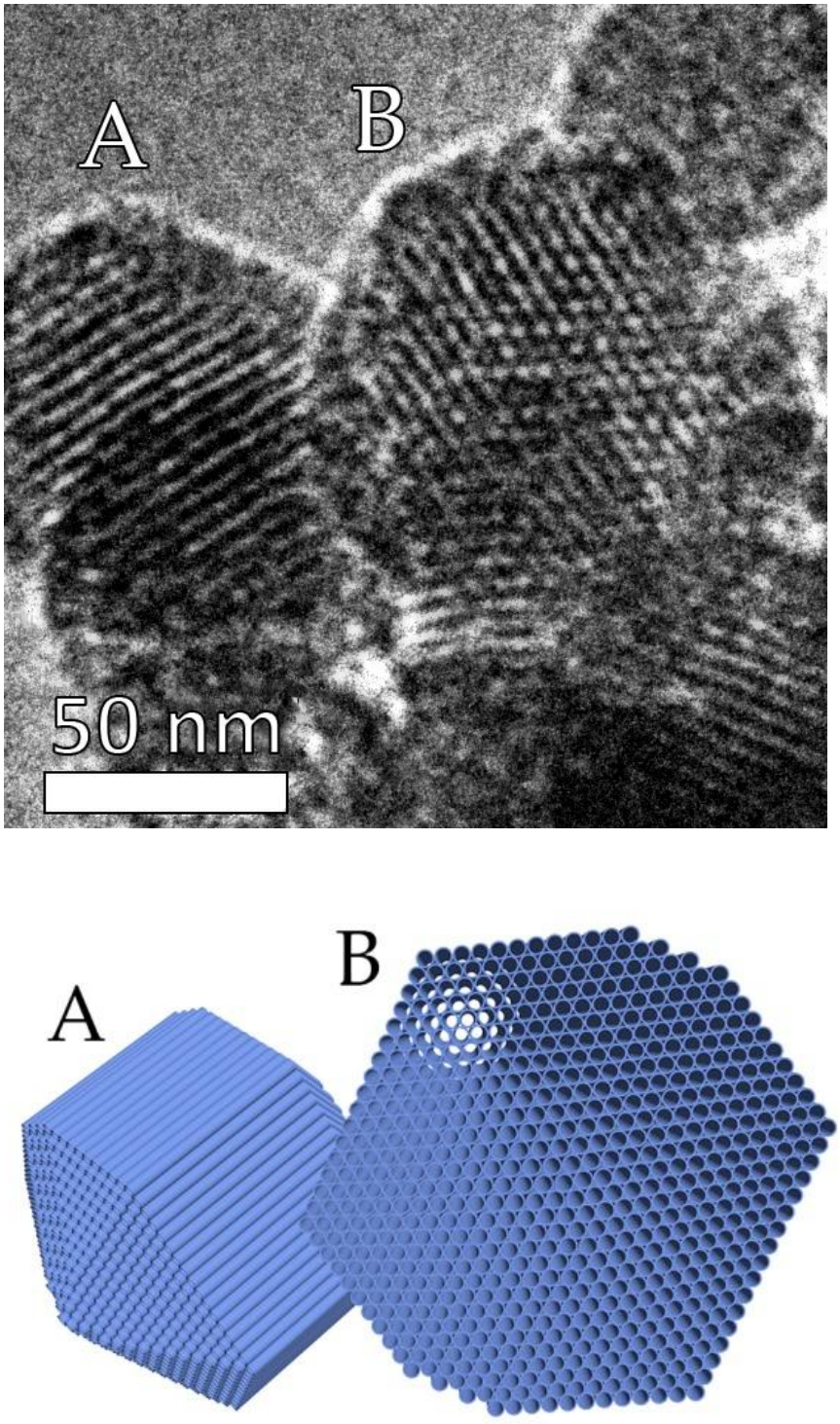

Figure 26. Top: TEM image of calcined Al-MCM-41; A - channels shown perpendicular to the line of vision; B - Channels shown parallel to the line of vision; Bottom: schematic illustration of the particle A and B.

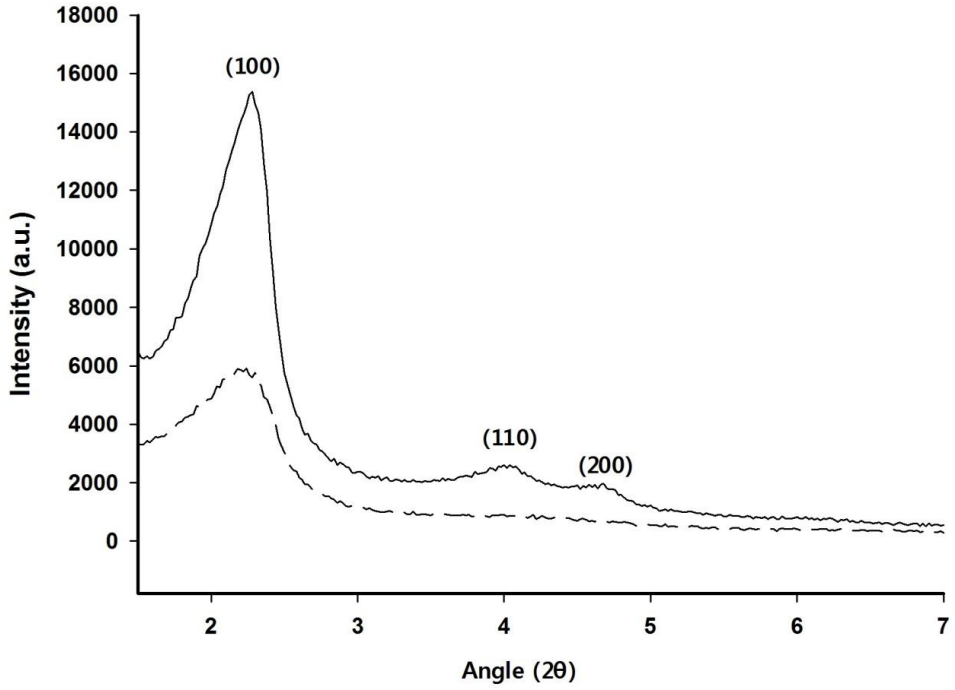

Figure 27. Solid line represents the calcined Al-MCM-41 XRD pattern of {Mn-CO}@Al-MCM-41 is the dotted line.

The pore diameter is calculated from a_o by subtracting 1.0 nm, which is an approximated value of the pore wall thickness.[41]The interplanar distance in the (100) direction, d_{100}, was calculated by Bragg's law ($n\lambda = 2d\sin\theta$). With the d_{100} value of 3.606 nm, the pore diameter is calculated to be 3.16 nm. (100) and (200) peaks are possibly broadened due to condensation of silanols during the calcination.[46]

5.3.2 Mn-qpa LOADING

The dotted line in Figure 27 is the XRD pattern of Al-MCM-41 after loading Mn-pqa compound. The most obvious difference is the loss of the (110) and (200) peaks. This is due to a loss of contrast from the filling of the pore voids.

However, the (100) peak is still relatively intense, meaning the mesoporous MCM-41 scaffolding is not damaged.[46]

Figure 28 shows a IR spectra comparison between Al-MCM-41 before and after loading Mn-pqa. While the two spectra look similar, there is a distinctive band stretching at ~2030 cm^{-1} for {Mn-CO}@Al-MCM-41 . It corresponds to the facially capping CO group of the carbonyl.[25] There is another CO stretching frequency in the region of 1930-1950 cm^{-1}, but it overlaps with the empty Al-MCM-41 's IR band. Thus, the band at ~2030 cm^{-1} was mainly used to confirm the Mn-pqa loading.

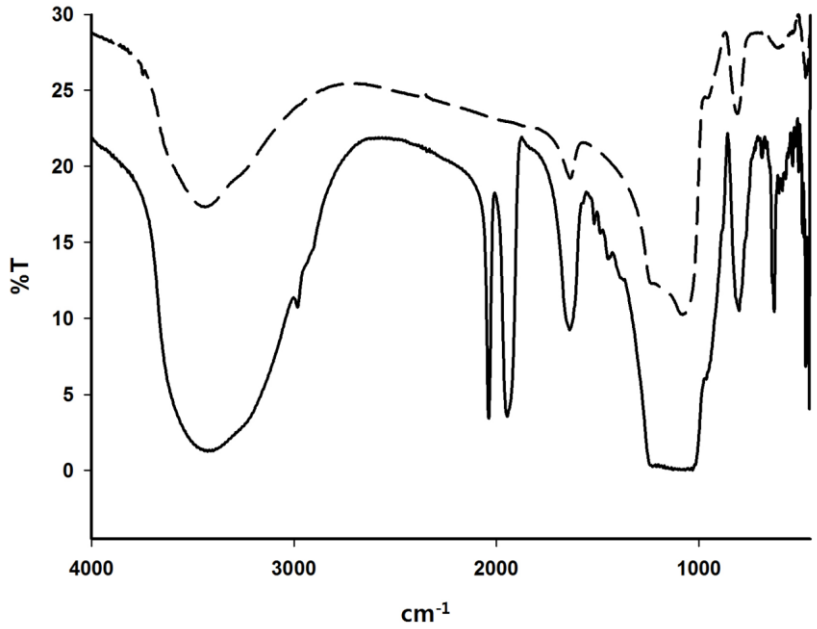

Figure 28. Dotted line is IR spectrum of empty Al-MCM-41 and the solid line is Al-MCM-41 after loading.

The actual amount of Mn-pqa loaded into Al-MCM-41 was determined by an acid digestion followed by analysis of the Mn content of the digest solution by ICP-OES. The composition of the loaded silicate material was determined to be ~2.06 wt% Mn.

SEM-EDX elemental mapping was performed to examine the incorporation of Mn-pqa into the porous Al-MCM-41 structure in order to examine how the guest molecules are distributed in the particles. Figure 29 shows the cross-sectional SEM-EDX elemental (Si, O, Al, and Mn) maps of {Mn-CO}@Al-MCM-41 particles. These maps confirm even distribution of Mn-pqa throughout the interior of the Al-MCM-41 particles. The even spread of Mn across the entire area of the particle indicates that the length of the channels is fully accessible to the diffusing guest molecules and do not become significantly blocked during the loading process.

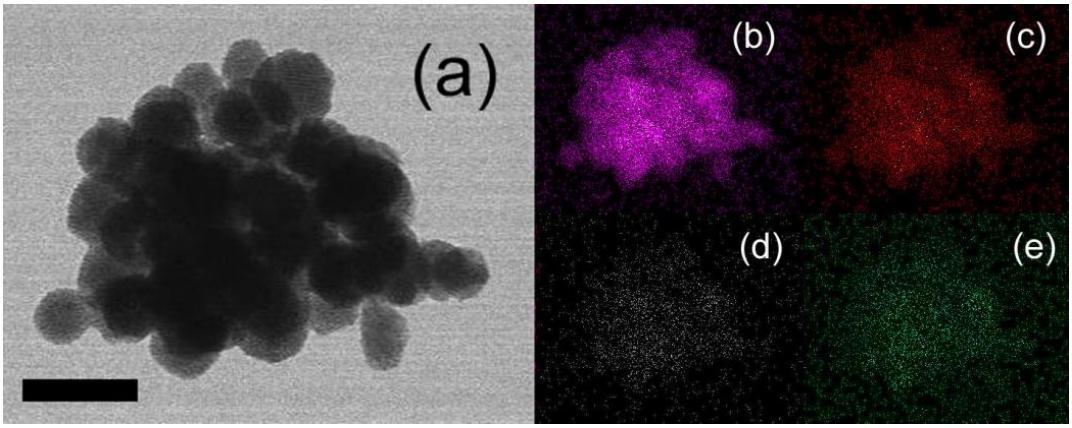

Figure 29. SEM elemental maps of Al-MCM-41 after loading: (a) TEM; (b) Si; (c) O; (d) Al; (e) Mn.

The loading of Mn-pqa is also evident in the TEM image. Figure 30a and b show the close-up TEM images of {Mn-CO}@Al-MCM-41. It is noticeable that the contrast is lower compared to the empty Al-MCM-41 shown in (c). For instance, the particle on the right is showing the channels parallel to the line of vision. Its contrast is relatively weaker compared to the middle particle, showing

channels perpendicular to the line of vision, because the pores of {Mn-CO}@Al-MCM-41 are blocked out by the Mn-pqa compounds. If the particles were just adsorbed onto the surface of the Al-MCM-41 particle, the image of hexagonal arrays should not lose contrast regardless of the viewing angle.

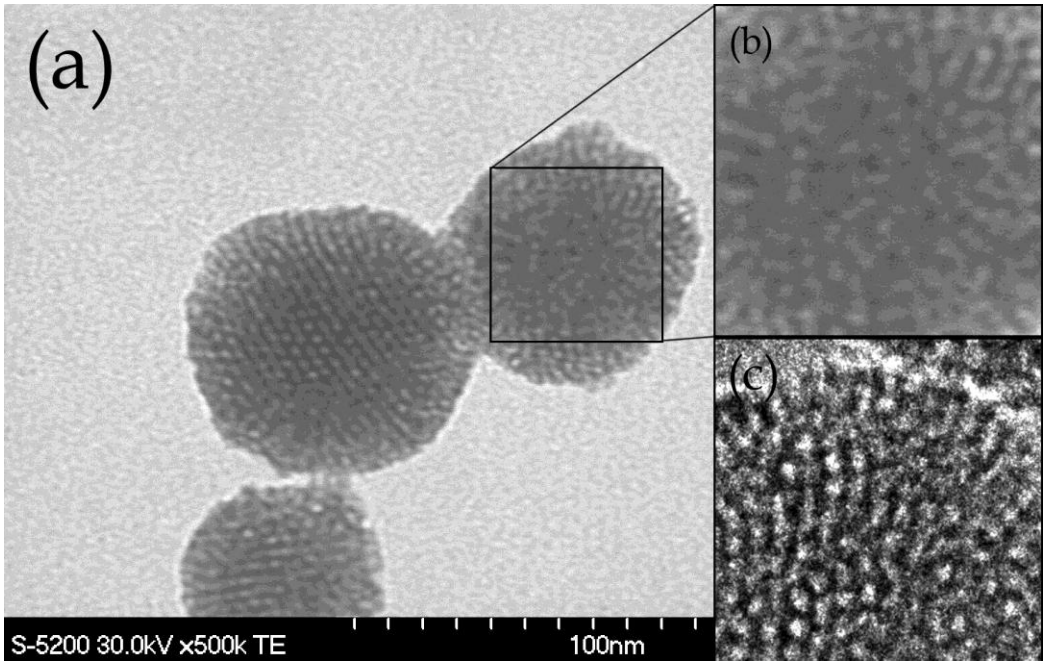

Figure 30. (a) TEM image of {Mn-CO}@Al-MCM-41; (b) magnification of one of the particles in (a); (c) TEM image of an empty Al-MCM-41 particle, in the same approximate orientation of (b).

The binding strength of Mn-pqa to the framework of the Al-MCM-41 was tested by measuring the extent of leaching of Mn-pqa from the porous structure in a physiologically relevant phosphate buffer (pH 6.5). In this experiment, the loaded materials were soaked in the buffer solution and gently agitated for 10 minutes. At different time intervals, 0.5 mL of the solution was diluted to 1.2 mL, filtered with syringe filter, and then measured by UV-Vis. After ~13 hours of soaking, {Mn-CO}@Al-MCM-41 lost ~0.27% of the total entrapped guest molecules (Figure 31). These values are normalized with respect to the total

amount of entrapped guest molecules in the materials. At the end of the 24 h period, the sample lost 1.83% of the guest molecule.

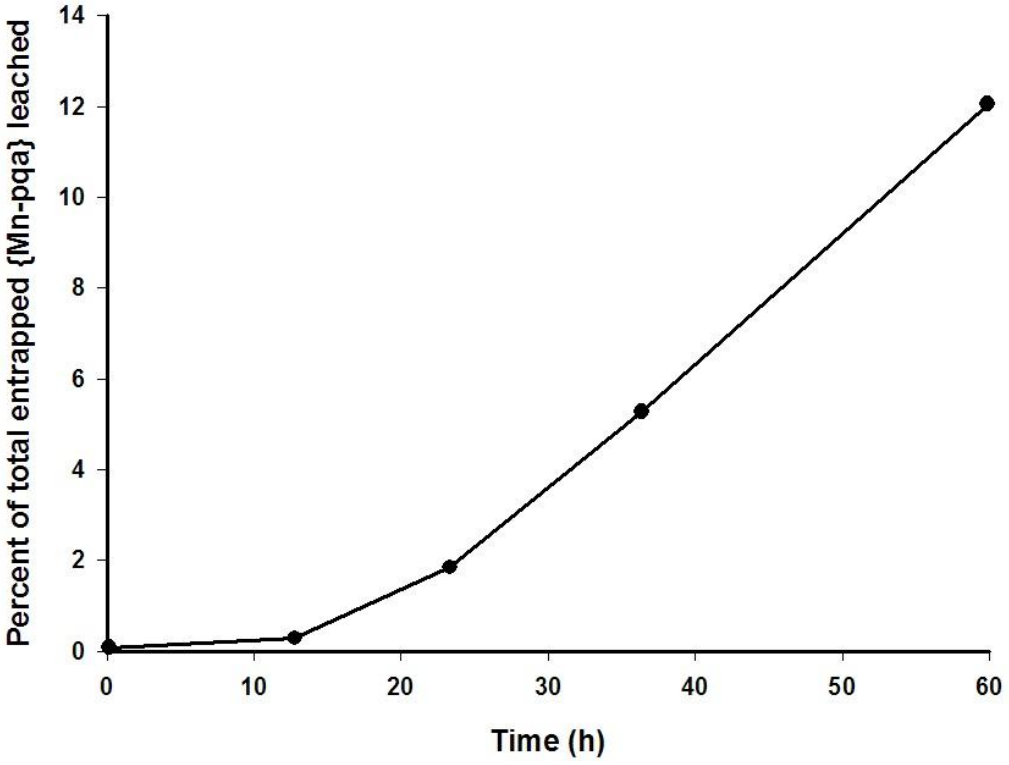

Figure 31. Leaching of Mn-pqa from Al-MCM-41 during soaking in phosphate buffer, measured by UV-VIS. The percentage was obtained by normalizing the measured amount of leached Mn-pqa to the total amount of Mn-pqa present in the sample.

5.3.3 CO Release

The release of CO from {Mn-CO}@Al-MCM-41 was confirmed by means of a myoglobin (Mb) assay according to the method reported by Motterlini *et al.*[22] In this study, conversion of deoxymyoglobin (deoxy-Mb) to carbonyl myoglobin (MbCO) was observed by looking at the time-dependent change in Q-band of the UV-Vis spectrum.

Once deoxy-Mb was prepared, {Mn-CO}@Al-MCM-41 was added to the solution with minimum agitation in order to reduce any leakage of $[Mn(pqa)(CO)_3]ClO_4$ from {Mn-CO}@Al-MCM-41. Once all the particles settled to the bottom, they were exposed to a broadband UV light source (λ >350 nm) at specific time intervals until all the deoxy-Mb has been converted to carbonyl-Mb. In Figure 32, a significant increase in the intensity of the α(~542 nm) and β(578 nm) Q-band are observed in the UV-vis spectrum, characteristic of carbonyl-Mb formation from an exogenous CO source.

Although the myoglobin assay we performed was not quantitative, future studies utilizing {Mn-CO}@Al-MCM-41 as a light-activated CO-donating material are possible, given that the extinction coefficients of both deoxyMb and carbonyl-Mb have been reported.[22]

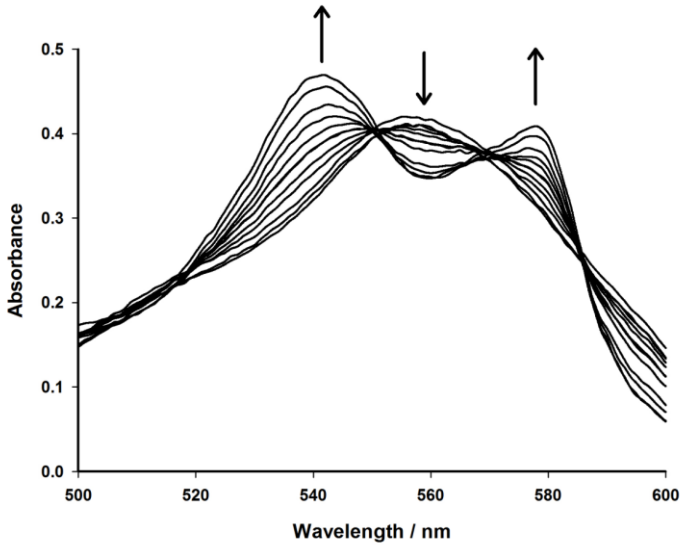

Figure 32. Detection of light-triggered CO release by monitoring the changes of the Q-band region of the UV-Vis spectra of reduced horse skeletal muscle myoglobin in the presence of Al-MCM-41 .

5.3.5 CELL VIABILITY

The biocompatibility of both Al-MCM-41 and {Mn-CO}@Al-MCM-41 were studied using HeLa cells as a model. Pre-cultured HeLa cells on 96-well plates were treated with different concentrations of nanoparticles: 10 25 50 and 100 µg/mL and 0 µg/mL as a control group. Then the cells were incubated for 6 hours in a humidified atmosphere (5% CO_2, 35 °C). After 6 h, the media in each well was aspirated and cell viability was assessed with a 3-(4,5-dimethylthiazol-2-yl)-2,5-diphenyltetrazolium bromide (MTT) assay, modified from the procedure by Dinischiotu and co-workers.[48] Fresh DMEM (150 µl) was added to each well, followed by 50 µl of MTT (5 mg/ml) in PBS. The cells were incubated for 2 h at 37℃ to allow for metabolism of formazan dye by viable cells. The media containing unreacted MTT solution was then removed by aspiration and 50 uL of DMSO was added and the plate shaken to dissolve the formazan crystals. The optical density at 595 nm was taken using a plate reader (VersaMax ELISA Microplate Reader, Molecular Devices, LLC.) Absorbance corresponding to the control (untreated) cells was referenced as 100% cell viability. Results presented in Figure 34 are the average of two independent trials.

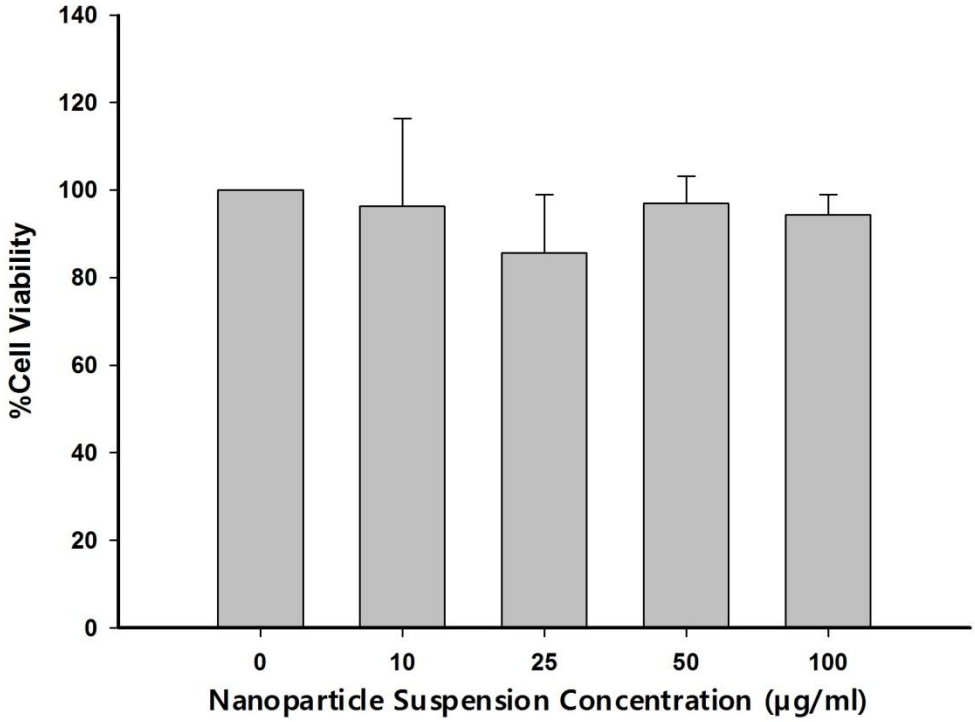

Figure 33 Hela viability after 6 hr incubation with loaded Al-MCM-41 .

According to the result obtained, the effect of Al-MCM-41 and {Mn-CO}@Al-MCM-41 did not significantly alter the cell viability. Also, no evident pattern related to the concentration was observed. However, for empty Al-MCM-41 , the relative cell viability for each concentration were consistent for each trial. Overall, a maximum of 15% decrease in cell viability was observed in the range of particle loadings examined for both loaded and unloaded Al-MCM-41. These preliminary results suggest the potential biocompatibility of our CO-donating material.

CHAPTER 6

CONCLUSION

Since the recognition of CO as a potential therapeutic agent, there has been much effort to develop more efficient ways to administer CO while minimizing its well-known toxicity. Use of metal carbonyls as CO delivering agent enabled more local administration of CO. We have attempted to further improve the overall performance in CO delivery by introducing a system with two major improvements. First is the use of photoactive CORM that is stable in physiological conditions. While previous CORMs, such as CORM-3 instantly released CO as it is exposed to a physiological condition, photoactivation allows us to release CO at desired time. Also, our photoCORM, Mn-pqa, utilizes near UV, which is easy and safe for clinical use. Encapsulation of CORM in MSN further improves our system's efficiency in several aspects. The major advantages from encapsulation is the ability to control the dosage and localization at a target site. The cells can uptake the nanoparticles with reasonable kinetics, and showed high viability regardless of the concentration of MSN used. Thus, CO can be released within the cell itself, allowing more direct administration compared to release of CO in the blood stream or on a tissue. Overall, this work has demonstrated a higher performance over traditional CO treatment, making it a promising next generation CO delivery system. In the future, more independent trials on TTM assays to study the "true" relationship between concentration of nanoparticles and cell viability, TEM image of HeLA cells with Al-MCM-41 uptaken, and numerical values for rate and amount of CO release vs. time exposure to light will be studied.

REFERENCE CITED

1. Oger, J. J. Neurol. Sci. **262** (1-2), 122–130.
2. Douglas, C. G., Haldane, J. S., and Haldane J. B. S. J Physiol. 1912, **44**(4), 275-304
3. Goldstein, M. J Emerg Nurs. 2008, **34**(6), 538-542
4. Motterlini, R.; Otterbein, L. E. Nat. Rev. Drug Discov. 2010, **9**, 728−743.
5. National Institutes of Health Clinical Center, Carbon Monoxide to Prevent Lung Inflammation. http://www.clinicaltrials.gov/ct2/show/NCT00094406 (1 May 2013).
6. Gref, R.; Minamitake, Y.; Peracchia, M.T. *et al*. Science 1994, **263,** 1600 - 1603 .
7. Tenhunee, R.; Marver, H.S.; Schmid, R.; Biochemistry 1968, **61**, 748
8. Maines, M.D.; Kappas, A. Biochem. J. 1976, **154**, 125-131
9. Maines, M.D.; Trakshel, G.M.; Kutty, K. K. 1986, **261**(1), 411-419
10. McCoubrey, W. K.; Huang, T. J.; Maines M.D. Eur. J. Biochem. 1997,**247**, 725-732
11. Gale, E.; Torrance, J.; Bothwell, T. J. Clin. Invest. 1963, **42**,7
12. Burg, R. V. J Appl Toxicol 1999, **19**, 379-386
13. Ryter, S. W.; Alam, J.; Choi, A. M. K. Physiol Rev. 2006, **86**, 583-650
14. Furchogott, R.F.; Jothianandan, D. Blood Vessels 1991, **28**(1-3), 52-61
15. Brouard, S.; Otterbein, L. E.; Anrather, J.; Tobiasch, E.; Bach, F. H.; Choi, A. M., and Soares, M. P. J Exp Med 2000,**192**, 1015–1026
16. Petrache, I.; Otterbein, L. E.; Alam, J.; Wiegand, G.W.; Choi A. M. Am J Physiol Lung Cell Mol Physiol 2000, **278**, L312–L319
17. Thom, S. R.; Fischer, D.; Xu, Y. A.; Proc Natl Acad Sci 2000, **97**, 1305–1310
18. Otterbein, L. E.; Bach, F.H.; Alam, J.; Soares, M.; Tao, Lu H.; Wysk, M.; Davis, R. J.; Flavell, R. A.; and Choi, A. M.; Nat Med 2000, **6** ,422–428

19. Otterbein, L. E.; Zuckerbraun, B. S.; Haga M.; Liu, F.; Song, R.; Usheva, A.; Stachulak, C.; Bodyak, N.; Smith, R. N.; Csizmadia, E.; Tyagi, S.; Akamatsu, Y.; Flavell, R. J.; Billiar, T. R.; Tzeng, E.; Bach, F. H.; Choi, A. M,; and Soares, M. P. Nat Med 2003, **9**,183–190

20. Song, R.; Mahidhara, S.; Zhou, Z.; Hoffman, R. A.; Seol, D. W.; Flavell, R. A.; Billiar, T. R.; Otterbein, L. E.; and Choi, A. M.; J Immunol 2004, **172**, 1220–1226

21. Herrmann W. A. J Organomet Chem. 1990, 383, 21–44

22. Motterlini, R.; Clark, J. E.; Foresti, R.; Sarathchandra, P.; Mann, B. E.; Green, C. J. Circ Res. 2002, **90**, e17-e24

23. Mann, B. E. Organomettalics 2012, **31**, 5728-5753

24. Clark, J. E.; Naughton P.; Shurey S.; Green C. J.; Johnson T. R.; Mann B. E.; Foresti R.; Motterlini R. Circ Res 2003, **93**, e2-e8

25. Gonzales, M. A.; Lim M. A.; Cheng, S.; Moyes, A.; Hobbs A. J.; Mascharak, P. K.; Inorg. Chem 2012, **51**, 601-608

26. Gref R.; Minamitake Y.; Peracchia M. T.; *et al*. Science 1994, **263**, 1600 – 1603

27. Vallet-Regí M.; Balas F.; Arcos D. Angew. Chem. Int. Ed. 2007, **46**, 7548 – 7558

28. Lu J.; Liong M.; Zink H. I. Small, 2007, **3**(8) 1341-1346

29. Hah, H. J.; Kim, J. S.; Jeon, B. J.; Koo, S. M.; Lee, Y. E Chem Commun 2003, 1712-1713

30. Caruso, F.; *et al* Science 1998, **282**, 1111

31. Rösler, A.; Vandermeulen G. W.; Klok H. A. Adv Drug Deliv Rev, 2001, **53**(1), 95-108

32. Patri, A. K.; Majoros I. J.; Baker Jr. J. R. Curr Opin Chem Biol 2002, **6**(4), 466-471

33. Qu, F,; Zhu, G.; Huang, S.; Li, S.; Sun, J.;Zhang, D.; Qiu, S. Microporous Mesoporous Mater, 2006, **91**, 1-9

34. Horchajada, P.; Rámila, A.; Pérez-Pariente, J.; Vallet-Regí, M. Microporous

Mesoporous Mater, 2004, **68**, 105-109

35. Lu, F.; Wu, S. H.; Hung, Y.; Mou, C.Y. Small, 2009, **5**(12), 1408-1413

36. Osaki, F.; Kanamori, T.; Sando, S.; Sera, T.; Aoyama, Y. J Am Chem Soc 2004, **126**, 6520-6521

37. Jiang, W.; Kim, B. Y. S.; Rutka, J. T.; Chan W. C. W. Nat. Nanotechnol. 2008, **3**, 145-150

38. Chithrani, B. D.; Chazani A.A.; Chan, W. C. W Nano Lett, 2006, **6**(4), 662-668

39. Beak, J. S.; Vartuli, J. C.; Roth, W. J.; Leonowicz, M. E.; Kresge, C. T.; Schmitt, K. D.; Chu, C. T. W.; Olson, D. H.; Sheppard, E. W. J Am Chem Soc 1992, **114**(27), 10834-10843

40. Vallet-Regi, M.; Rámila, A.; del Real, R. P.; Pérez-Pariente, J., Chem Mater, 2001, **13**(2), 308-311

41. Cai, Q.; Luo, Z. S.; Pang, W. Q.; Fan, Y. W.; Chen, X. H.; Cui, F. Z., Chem Mater, 2001, **13**, 258-263

42. Lee, H.; Pinto J. M.; Grossmann, I. E.; Park, S., Ind Eng Chem Res 1996, **25**, 1630-1641

43. Heilman, B. J.; St. John, J.; Oliver, S. R. J.; Mascharack, P. K, J Am Chem Soc 2012, **134**(28), 11573,11582

44. Aspromonte, S. G.; Sastre, Á.; Boix, A. V., Cocero, M. J.; Alonso, E. Microporous and mesoporous Mater, 2012, **148**, 53-61

45. Chao, K. J.; Chen, S. H.; Yang, M. H. Anal Chem 1988, **331**, 418-422

46. Aznar, E.; Marcos, M. D.; Martínez-Máñes R.; Sancenón F.; Soto, J.; Amerós, P.; Guillem C. J AM Chem Soc, 2009, **131**(19), 6833-6843

47. R. Motterlini, R.;Clark, R. Foresti, P. Sarathchandra, B. E. Mann, C. J. Green, Circ. Res.2002, 90, e17 – e24.

48. Dinu, D.; Bodea, G. O.; Ceapa, C. D.; Munteanu, M. C.; Roming, F. I.; Serban, A. I.; Hermenean, A.; Costache, M.; Zarnescu, O.; Dinischiotu, A.,Toxicon, 2011, **57**, 1023-1032.